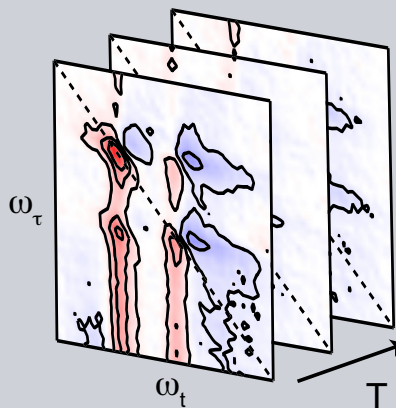**Abstract** Optical multidimensional coherent spectroscopy (MDCS) is a nonlinear spectroscopy technique where a material is excited by a series of laser pulses to produce a spectrum as a function of multiple frequencies. The technique's ability to elucidate excited-state structure and interactions has made MDCS a valuable tool in the study of excitons in semiconductors. This review introduces the method and describes progress it has fostered establishing a better understanding of dephasing rates, coherent coupling mechanisms, and many-body interactions pertaining to optically generated electronic excitations in a variety of semiconductor material systems. Emphasis is placed on nanostructured gallium arsenide quantum wells and quantum dots, on quantum dots in other III-V and II-VI semiconductors, and on atomically thin transition metal dichalcogenides. Recent technical advances and potential future directions in the field are also discussed.

Multidimensional Coherent Spectroscopy of Semiconductors

Christopher L. Smallwood[1,2] and Steven T. Cundiff[1,*]

1. Introduction

This review highlights the progress being made in understanding the physics of light-matter interactions in semiconductors using optical multidimensional coherent spectroscopy (MDCS). Although the roots of MDCS can be traced to the development of two-dimensional nuclear magnetic resonance (2D-NMR) by Ernst and collaborators in the 1970s [1], advances in both laser development and interferometric stabilization have pushed the technique far beyond its radio-frequency origins, extending it into the infrared regime [2], the optical regime [3–5], and in a few recent cases even into the ultraviolet [6]. Today, optical MDCS (with a wavelength range of 400–1000 nm) has emerged as a powerful method for studying properties ranging from many-body dynamics in semiconductors [7–10] to energy-transfer processes in photosynthetic light harvesting complexes [11,12] to interactions and dynamics in atomic and molecular vapors and solutions [13–15].

The application of MDCS to semiconductors has proved illuminating because the most prominent semiconductor excitations are excitons, which are neutrally charged electron-hole bound states [16,17]. Because excitons lack charge, they are hard to study using the traditional methods of electron transport. Within the realm of optically accessible momenta, however, the same bound-state interaction also restricts the allowed energies to discrete values, making excitons ideal subjects of study using MDCS. Beyond this, the proximity of electrons and holes in typical excitons gives them larger dipole moments than their unbound counterparts and marks them as one of the most important

actors in all-optical processes [18]. In the case of atomically thin transition metal dichalcogenides (TMDs), the excitonic light-matter interaction can dominate a semiconductor's response such that the impact of free carriers is entirely obscured [19].

The review is organized into six sections. In Section 2, we present a tutorial on multidimensional coherent spectroscopy, summarizing the mechanics and intuition behind coherent spectroscopy techniques, explaining the basic features of MDCS plots and how to interpret them, and giving a short review of modeling techniques in the perturbative limit. Sections 3, 4, and 5 summarize the progress and impact that MDCS has had in developing a better understanding of the physics behind coherent interactions in quantum wells (Section 3), quantum dots (Section 4), and TMDs (Section 5). Finally, Section 6 discusses the field's future by summarizing progress in the study of new materials and outlining possibilities for improving spectrum acquisition time, spatial resolution, and frequency resolution.

2. Tutorial on the multidimensional coherent spectroscopy technique

A multidimensional coherent spectrum is a map of coherent light-matter interactions plotted across a domain of two or more frequencies. Such a spectrum is obtained by illuminating a material with a series of electromagnetic pulses and analyzing the frequency-dependent way in which excitation of the sample by the initial or intermediate pulses affects the material's response to the final pulses.

[1] Department of Physics, University of Michigan, Ann Arbor, MI 48109
[2] Present address: Department of Physics & Astronomy, San José State University, San Jose, CA 95192
[*] Corresponding author: e-mail: cundiff@umich.edu
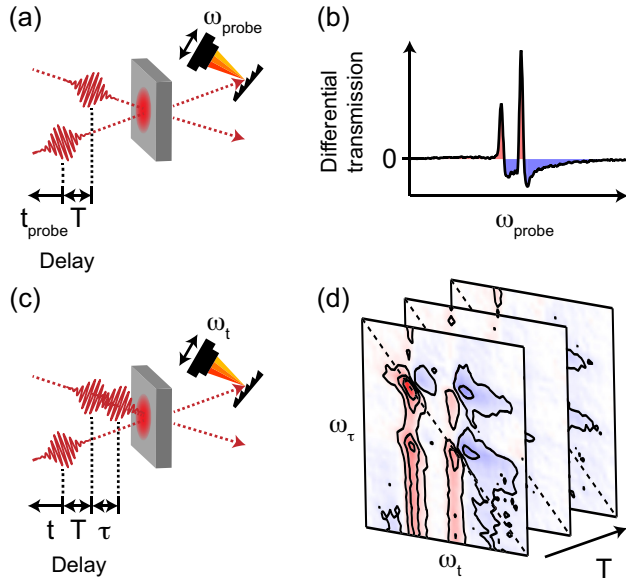
Figure 1 Comparison between transient absorption spectroscopy and MDCS. **(a)** In transient absorption spectroscopy, the differential transmission of an optical pulse (the "probe") is measured in response to the application of an earlier pulse (the "pump"). The pulses are delayed with respect to each other by a time T. **(b)** For a given T, the response may be plotted as a spectrally resolved function of the probe frequency ω_{probe}. **(c)** In a simple implementation of MDCS, the pump pulse from (a) is divided into sub-pulses, defining an additional time delay τ. **(d)** Data may be acquired as a function of varied τ and/or T, and Fourier-transformed to produce spectra with multiple frequency axes.

Perhaps the simplest way to understand the technique is as an extension of transient absorption spectroscopy, as illustrated by Fig. 1. In a transient absorption experiment [Fig. 1(a)], a sample is illuminated by two pulses. The first of these (the "pump") drives the sample into a nonequilibrium state, which is then measured by subtracting the sample's response to the second pulse (the "probe") in the pump's presence from the response to the probe in the pump's absence. The resulting differential signal can be measured as an integrated quantity using a photodiode or, by sending the output signal into a spectrometer, as a spectrally resolved quantity plotted against the probe frequency [Fig. 1(b)].

In order for a signal to be observed, some form of optical nonlinearity must be present. The most straightforward of these is saturation, in which the pump pulse decreases the sample's net absorption of the probe pulse, thereby generating a positive signal in differential transmission. For interacting many-body systems there are also other possibilities. For example, the pump can broaden the linewidth of the sample's response to the probe pulse (excitation-induced dephasing, or EID), which tends to produce positive central peaks with negative wings. It can also shift the center frequency of the resonance (excitation-induced shift, or EIS), creating asymmetric pump-probe signals. The effects of both EIS and EID are visible in Fig. 1(b), which corresponds to an asymmetric $In_{0.05}Ga_{0.95}As$ double quantum
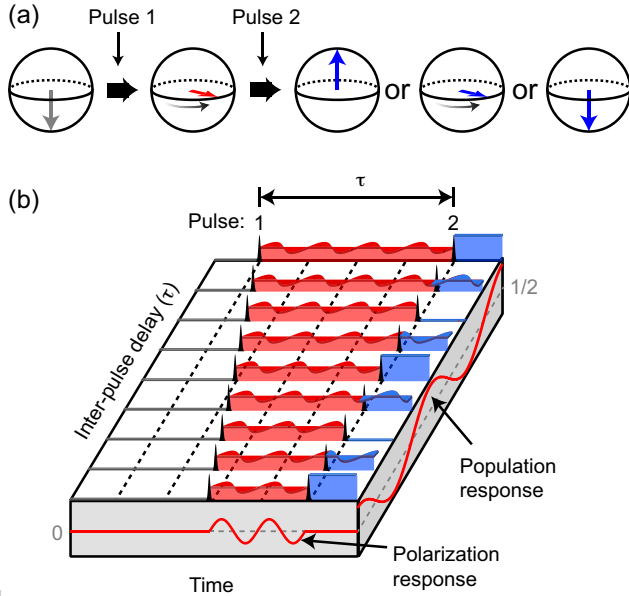
well where many-body effects are known to dominate the optical response.

Although it improves upon the information available through linear absorption, transient absorption is still incomplete because the sample's response to the pump pulse remains unknown even as its differential probe-pulse response is spectrally resolved. In part because of this limitation, results are often obscured in the presence of inhomogeneity resulting, for example, from sample imperfections, variations in confinement potentials, or uneven strain. To remedy the situation, the pump may be divided into a pair of sub-pulses [Fig. 1(c)]. The inter-pulse delay between these (τ) can then be systematically varied, and the data can be numerically Fourier-transformed to obtain a spectrally resolved excitation axis. The delay between the second and third pulses (T) tracks the pump-probe delay. The third pulse continues to act as a probe, leading to a differential response that is either emitted from the sample over an elapsed time (t) as coherent four-wave mixing, or converted by a fourth pulse (not shown) after time t into a signal in photoluminescence, photocurrent, or photoemission. The resulting MDCS plot is a time-resolved signal that is also frequency-resolved as a function of both excitation (pump) and emission (probe) frequency [Fig. 1(d)]. As we will show later on, unfolding the spectral response across these multiple frequency dimensions facilitates a wealth new capabilities, including the ability to disentangle microscopic dephasing in the midst of sample inhomogeneity, the ability to identify coherent coupling mechanisms between resonances, and the ability to more thoroughly constrain the mechanisms behind many-body interactions.

2.1. Coherent spectroscopy

One might wonder, based on the schematic depicted in Fig. 1(c), how coherent information related to the sample's response to pulse 1 can possibly be extracted from the final measurement. After all, the sample's response to the probe pulse is ultimately the only signal measured. The issue is resolved by noting that if time delays between pulses are controlled with sub-wavelength precision, then coherent interactions from the earlier pulses will be written into the phase of measured signal later on.

A simple illustration of the effect is shown in Fig. 2, depicting a Bloch sphere illustration [20] of a two-pulse correlation measurement in which $\pi/2$ pulses are applied to a two-state system. As illustrated by Fig. 2(a), the system is initially in the ground state such that the Bloch vector points downward for times $t < 0$ [Fig. 2(a), left]. At $t = 0$, a $\pi/2$ pulse is applied, driving the system into a coherent superposition of the ground and excited states. The superposition evolves with time [Fig. 2(a), center], rotating around the Bloch sphere's equator until it dephases and relaxes back down into the ground state, or until (as illustrated) a second $\pi/2$ pulse is applied. Depending on the relative delay and phase difference between these two pulses, the second pulse can drive the system into a ground-state population, an

(a) Pulse 1 Pulse 2 or or

(b) τ

Pulse: 1 2

1/2

Inter-pulse delay (τ)

Population response

Polarization response

0

Time

Figure 2 Coherent spectroscopy of a two-level system in the $\pi/2$-pulse limit. **(a)** Bloch sphere illustration of the quantum state's evolution. The system is initialized in the ground state (left), driven into a superposition between ground and excited states by the a $\pi/2$ pulse (center), and converted into a potential variety of population states and superposition states by a second $\pi/2$ pulse (right). **(b)** Varying the time delay between the two pulses maps the intermediate quantum state's coherent evolution (horizontal red oscillations, center) onto the final state's excited-state population (vertical blue projections and red oscillations, right).

excited-state population, or anywhere in between [Fig. 2(a), right].

When the delay and phase relationship between pulses 1 and 2 is controlled with sufficient precision, the model illustrates a striking feature of the response, as shown in Fig. 2(b). Even though the second pulse fundamentally alters the intermediate quantum state, and in cases converts the superposition between the ground and excited state into a population state without oscillatory motion, the information about the intermediate state still gets written onto the final state's dependence on interpulse delay. This dependence can be seen in the red trace on the right side of Fig. 2(b), which tracks oscillations in the population component of the final quantum state.

It is worth noting that the Bloch sphere example differs from a typical optical coherent spectroscopy experiment in one significant respect. Whereas the example from Fig. 2 employs $\pi/2$ pulses, the pulses much more commonly employed in MDCS are perturbative. Nevertheless, the key aspects of the illustrated pathway remain a valid description of the measured portion of the perturbative response function. The connections are solidified in Section 2.4.

## 2.2. Multidimensional coherent spectroscopy

With two-pulse correlation spectroscopy established, the technique can be readily extended to encompass light-matter interactions involving three, four, and in some cases even more pulses, producing spectral information against multiple frequency dimensions. A characteristic example of an MDCS plot is depicted in Fig. 3, showing coupled exciton resonances in an asymmetric InGaAs double quantum well.

As shown by Fig. 3(a), the spectrum is generated by exciting the sample with three optical pulses to create a nonlinear polarization response (green oscillations). The response can either be measured as heterodyne-detected four-wave mixing, as was the case for the data in Fig. 3, or it can be converted by a readout pulse into a higher-order population response that can be detected as a photocurrent, photoluminescence, or photoemission signal. Detailed accounts of detection schemes and phase-stabilization methodology have been discussed in Refs. [2–4, 7, 9, 10, 15, 21], which review the MDCS technique from complementary perspectives. Regardless of detection scheme, the time delay between pulses 1 and 2 is then varied to produce a two-dimensional plot of the response as a function of excitation time τ and emission time t as displayed in Fig. 3(b), plotted in a rotating frame. The frequency-domain data [Figs. 3(c)–3(e)] correspond to the Fourier-transform of the time-domain data in Fig. 3(b). The excitation axes have negative frequency units for reasons to be explained in Section 2.3.

Figures 3(c)–3(e) exhibit a number of features that illustrate the power of MDCS as an experimental technique. Prominent features are two peaks along the diagonal, where $|\omega_\tau| = |\omega_t|$. Such features are analogous to what might be observed using a simpler method such as one-dimensional absorption or photoluminescence, and originate from energetically degenerate interactions where the pump pulse excitations induce a change in the probe pulse interaction at the same frequency. The frequencies of the diagonal peaks can be used to determine the quantity and spacing of a system's excited states. Ratios between peak heights can be used to determine relative optical absorption strength.

The diagonal peaks in an MDCS experiment provide more information than their one-dimensional counterparts in absorption, photoluminescence, and transient absorption. For example, the resonances in Fig. 3(c) are elongated, which is a consequence of the fact that sample inhomogeneities create variations in a quantum well's local environment. In a one-dimensional measurement, these variations smear resonance characteristics out, making it hard to ascertain the microscopic dephasing times within the larger macroscopic ensemble. By contrast, an inhomogeneously broadened feature in an MDCS spectrum remains narrow along the perpendicular "cross-diagonal" direction almost independently of the system's inhomogeneity, making quantitative measurements of intrinsic dephasing rates possible [22–24].

A more striking contrast between MDCS and one-dimensional measurements is that degenerate interactions can be separated from non-degenerate ones. For example, the Fig. 3(c) spectrum exhibits two "cross peaks" at (1462,-
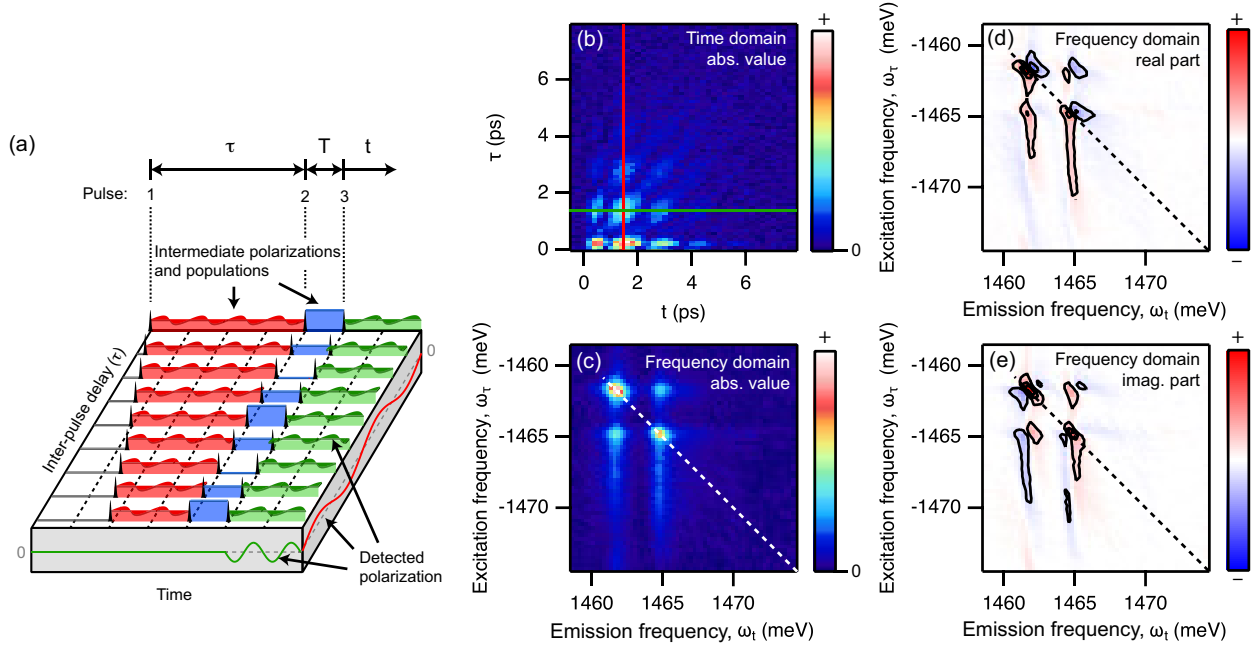
Figure 3 Mechanistic illustration of MDCS. **(a)** Varying the time delay τ (between pulses 1 and 2) while keeping the delays T (between pulses 2 and 3) and t (following pulse 3) fixed writes coherent pump-pulse absorption characteristics (red oscillations, center left) onto the output signal (red oscillations, bottom right). Tracking t at fixed τ and T gives coherent emission characteristics of the output signal (green oscillations, bottom front). **(b)** The result may be plotted as a two-dimensional function of four-wave mixing vs. τ and t. **(c–e)** Performing the Fourier transform of (c) produces a coherent frequency-resolved two-dimensional spectrum.

1464.9) meV and (1464.9,-1462) meV, which can arise for a number of reasons. If the two resonances share a common ground state, then the pump pulse interaction with one of the resonances can result in a ground-state bleaching, affecting the probe pulse's interaction at the frequency of the second resonance. The pump can also drive the system into a coherent superposition between the two excited states. In both cases, the detection of cross peaks constitutes a direct signature of coupling between the two resonances that would be more difficult to observe using simpler spectroscopic methods.

Finally, as shown by Figs. 3(d) and 3(e), the frequency spectrum is also phase-resolved. Analyses of the real and imaginary components of the signal and comparison to theoretical models can reveal important information about many-body effects and excitation-related interactions within the material sample. As discussed in Sections 3–5, the study of many-body effects has been perhaps the single greatest contribution of MDCS to the field of semiconductor physics.
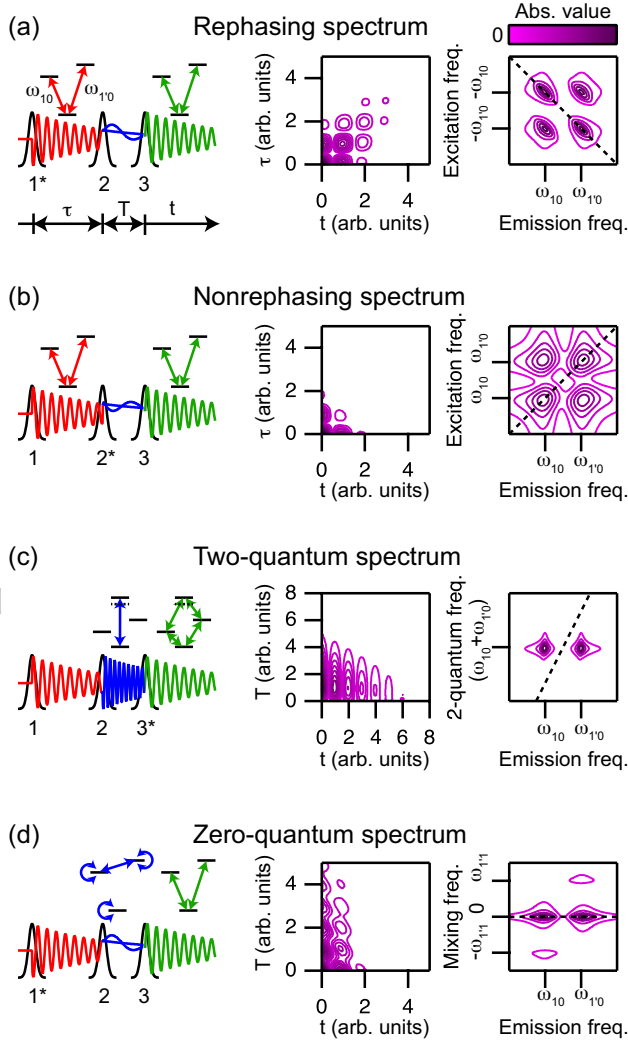
2.3. Spectrum classifications

Depending on pulse-ordering and signal detection filtering choices, different types of multidimensional spectra can be obtained from a material. Among the most common of these is the "rephasing" spectrum, which was depicted in Fig. 3, and which is illustrated for a simulated three-state "v" system in Fig. 4(a). Rephasing spectra are generated using an experimental configuration in which a material's interaction

with the first pulse is conjugate to its interaction with the second and third pulses. This can be achieved by arranging the excitation pulses to have distinct momentum vectors (e.g., $\mathbf{k}_1$, $\mathbf{k}_2$, and $\mathbf{k}_3$) and isolating a four-wave mixing signal at $\mathbf{k}_I \equiv -\mathbf{k}_1 + \mathbf{k}_2 + \mathbf{k}_3$ [25,26], by tagging the pulse trains with different carrier frequencies (ω_1, ω_2, and ω_3) to obtain a four-wave mixing signal at $\omega_I \equiv -\omega_1 + \omega_2 + \omega_3$ [27–30], and/or by phase cycling [1, 31]. In such a spectrum, the coherence generated by the first pulse is opposite in frequency to that generated by the third pulse, which is why the excitation frequencies in Figs. 3(c)–3(e) and in the right panel of Fig. 4(a) are negative. In turn, the pulse sequence tends to bring different resonances of an inhomogeneously broadened system into phase with each other during the emission process, resulting in the elongated "photon echo" signature [32] in the time domain spectrum of Fig. 4(a) (note the clustering of spectral intensity near emission times $t = \tau$), as well as the narrowed cross-diagonal lineshapes in the Fig. 4(a) frequency domain spectrum.

Spectra can also be collected from a conjugate second-pulse interaction relative to the interactions of the first and third pulses in a "non-rephasing" interaction [Fig. 4(b)], which can be achieved by collecting a four-wave mixing signal at $\mathbf{k}_{II} \equiv \mathbf{k}_1 - \mathbf{k}_2 + \mathbf{k}_3$ and $\omega_{II} \equiv \omega_1 - \omega_2 + \omega_3$. In this case, the phase difference between resonant interactions at different frequencies increases monotonically with time, resulting in a time-domain signal without a photon echo, and in time-domain and frequency-domain signals that are typically weaker than their rephasing counterparts. Nevertheless, the nonrephasing pulse sequence is still preferred over the

Figure 4 MDCS classifications with simulated data. Spectra correspond to the signal's absolute value, with linearly spaced contours. 2D time plots are in the rotating frame. **(a)** One-quantum rephasing spectrum for an inhomogeneously broadened three-state "v" system. **(b)** One-quantum nonrephasing spectrum for an inhomogeneously broadened three-state "v" system. **(c)** Two-quantum spectrum for a four-state diamond system. **(d)** Zero-quantum spectrum for an inhomogeneously broadened three-state "v" system.

rephasing pulse sequence in certain applications because the resonant peaks of a nonrephasing spectrum arise from slightly different physical origins and interfere differently with each other in close proximity than do the peaks of a rephasing spectrum [33–35]. Beyond this, if the real parts of rephasing and nonrephasing spectra are added together, one obtains a purely "absorptive" spectrum, which is perhaps the closest physical analog to the signals generated in transient absorption spectroscopy [36].

Figure 4(c) shows the spectrum from a pulse sequence in which the third pulse is conjugate relative to non-conjugate first and second pulses, achieved by collecting a four-wave mixing signal at $\mathbf{k}_{III} \equiv \mathbf{k}_1 + \mathbf{k}_2 - \mathbf{k}_3$ and

$\omega_{III} \equiv \omega_1 + \omega_2 - \omega_3$. The spectrum is commonly termed a two-quantum (or double-quantum) spectrum because it produces no signal except in the presence of a system with a doubly-excited state, for which a direct optical transition is often dipole-forbidden. Correlating the evolution time of the two-quantum coherence residing within the time interval T and the one-quantum coherence generated during time t is often powerful because it gives a background-free view into many-body interactions [37].

In analogy to two-quantum spectroscopy, it is also possible to generate correlation plots probing the mixing interaction between nearly degenerate quantum states using rephasing or nonrephasing pulse-ordering sequences, which is often just as inaccessible to optical techniques as the dipole-forbidden two-quantum coherence. Figure 4(d) shows an example of such a "zero-quantum" spectrum, for the rephasing pulse sequence from Fig. 4(a).

Finally, one can even generate three-dimensional coherent spectra, in which all three inter-pulse delays are varied to produce correlations three independent frequency domains [38]. Such 3D spectra provide perhaps the clearest separation of quantum pathways possible in an optical spectroscopic measurement, and although less common than their 2D counterparts, have been acquired on gallium arsenide quantum wells [39, 40].

2.4. Interpreting MDCS in the perturbative limit

Much of the preceding discussion becomes more concrete when framed in the context of semiclassical perturbation theory as applied to the Bloch model [41, 42]. Although the treatment of excitonic systems using a discrete level system such as this differs from theoretical treatments based on first-principles calculations involving fermionic creation and annihilation operators, the two pictures can be reconciled as discussed in Ref. [43]. In the Bloch model treatment, the material system's density matrix $\hat{\rho}$ is expanded as a perturbative series

$$\hat{\rho} = \hat{\rho}^{(0)} + \hat{\rho}^{(1)} + \hat{\rho}^{(2)} + \hat{\rho}^{(3)} + ... \qquad (1)$$

where each element of the series can be iteratively determined from lower-order elements according to the equation

$$\rho_{ij}^{(n)}(t) = \int_{-\infty}^{t} -\frac{i}{\hbar}[\hat{V}(t'), \hat{\rho}^{(n-1)}]_{ij} e^{-i\Omega_{ij}(t-t')} dt'. \qquad (2)$$

The complex resonance frequency

$$\Omega_{ij} \equiv \omega_{ij} - i\gamma_{ij}, \quad \text{with} \quad \omega_{ij} \equiv \frac{E_i - E_j}{\hbar}. \qquad (3)$$

The energies E_i and E_j are associated with eigenstates ρ_{ii} and ρ_{jj}, respectively, and γ_{ij} is a damping constant. The interaction Hamiltonian

$$\hat{V}(t) = -\hat{\mu} \sum_m \left[\mathscr{E}_m(t) e^{i(k_m x - \omega_m t)} + \text{c.c.} \right], \qquad (4)$$
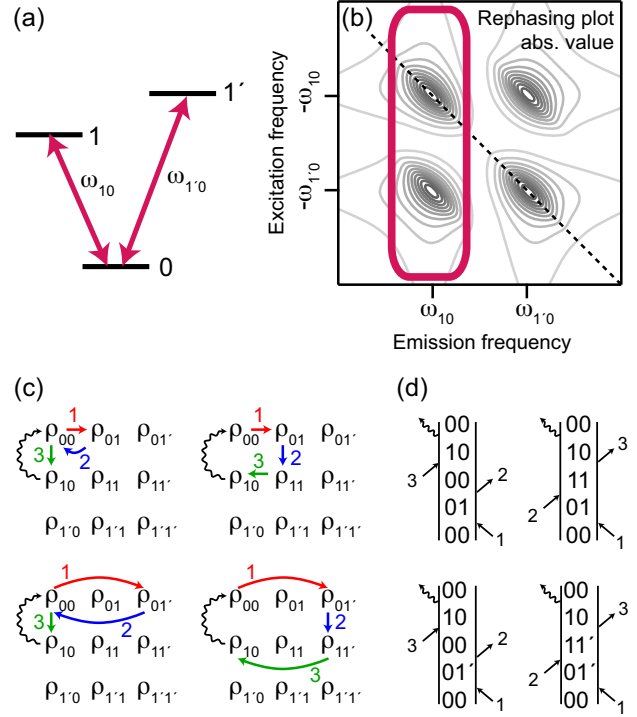
which is a sum of products between the material system's electric dipole moment operator $\hat{\mu}$ and the relevant optical modes, indexed by the subscript m.

We consider the nth-order perturbative regime to be the regime such that $\sum_{m=n+1}^{\infty} \hat{\rho}^{(m)} \ll \hat{\rho}^{(n)}$, which is a condition typically realizable at a desired order n by controlling the amplitudes $\mathscr{E}_m(t)$ of the interacting fields in Eq. (4). The task of modeling an MDCS spectrum then amounts to characterizing $\hat{\rho}$ to the highest relevant perturbative order and discarding all orders beyond this.[1] Because MDCS requires a minimum of three distinct optical interactions, the task reduces to the calculation of a subset of contributions to $\hat{\rho}^{(n \geq 3)}$ where the successive orders in perturbation theory leading up to the nth order correspond to exactly one interaction with each of the excitation pulses. These nth-order density matrix corrections ultimately emerge as measurable quantities such as the sample's macroscopic polarization (for off-diagonal elements) or excited-state population (for diagonal elements).

In general, the tabulation of the constituent elements—termed Liouville space pathways—of an element of an individual perturbative order is quite large. For three optical fields interacting with just a two level system, $\rho_{10}^{(3)}$ is already composed of 864 pathways. Fortunately, time ordering rules, the rotating wave approximation, wave vector selection rules, and frequency selection rules substantially reduce the number of pathways that are actually relevant.

An illustrative example of these simplifications is the determination of $\rho_{10}^{(3)}$ for the rephasing pulse sequence and three-state "v" system depicted in Fig. 4(a) [replicated in Figs. 5(a) and 5(b)]. The measured four-wave mixing signal has wave vector $\mathbf{k}_{sig} = -\mathbf{k}_1 + \mathbf{k}_2 + \mathbf{k}_3$ and frequency $\omega_{sig} = -\omega_1 + \omega_2 + \omega_3$, which requires the signal to emerge from at least one interaction each with each of the excitation pulses 1, 2, and 3. Because $\rho_{10}^{(3)}$ is a third-order correction, however, the interaction can also contain *no more* than one interaction each with each of these pulses. Time ordering dictates that the first-order interaction be the interaction with pulse 1, the second-order interaction be the interaction with pulse 2, and the third-order interaction be the interaction with pulse 3. Finally, the fact that the material's interaction with pulse 1 is conjugate to its interaction with pulses 2 and 3 means that the first-order interaction must be on the opposite side of the density matrix as the third-order interaction (i.e., the first-order interaction must be in the density matrix's first row). In all, this leaves only four contributions to $\rho_{10}^{(3)}$, illustrated schematically in Fig. 5(c). The upper pathways correspond to diagonal stimulated emission and bleach interactions in which the excitation pulse at $\omega_{01} = -\omega_{10}$ affects the detection pulse interaction at ω_{10}. The lower left pathway corresponds to a cross-peak bleach interaction

Figure 5 Graphical representations of Liouville space pathways in density matrix perturbation theory. **(a)–(b)** Diagrams are derived from a rephasing interaction between light and a three-state "v" system as depicted in (a), and correspond to contributions to $\rho_{10}^{(3)}$, generating the left two peaks in (b). **(c)** Matrix representations of the relevant Liouville space pathways where the red, blue, and green arrows correspond to first-, second-, and third-order interactions with the excitation beams, and the wavy black arrow corresponds to resulting coherent nonlinear emission. The upper pathways correspond to the upper left peak in (b). The lower pathways correspond to the lower left peak in (b). **(d)** Double-sided Feynman diagrams for the same interactions.

in which the excitation pulse interaction at $\omega_{01'} = -\omega_{1'0}$ affects the detection pulse interaction at ω_{10}. The lower right pathway corresponds to a zero-quantum stimulated-emission interaction in which the second pulse drives the system's second-order correction to $\hat{\rho}$ into a coherent superposition of states $|1\rangle$ and $|1'\rangle$.

The restriction of quantum pathways to taxicab-geometry patterns in Fig. 5(c) (that is, patterns where nth-order density matrix corrections are prohibited from incrementing diagonally upon corrections at order $n-1$) provides a convenient illustration of the fact that the structure of Eq. (2) requires the element $\rho_{ij}^{(n)}$ to share at least one of its indices with each of the elements of the lower-order density matrix correction $\hat{\rho}^{(n-1)}$ upon which $\rho_{ij}^{(n)}$ is generated. In turn, the illustration provides a physical justification for the common description of MDCS that the initial pulse creates a coherence in the sample, the second pulse converts the coherence into a population, and that the third pulse converts the population back into a coherence.

---

[1]   For collective systems the perturbative regime of the density matrix is more restrictive than the equivalent perturbative regime of the measured polarization. In many cases, however, the two approximations yield identical results, allowing experiments to be interpreted using only the density matrix ground state and first few excited states without difficulty [44].

As demonstrated by the cartoons and above discussion, the division of contributions to a given MDCS experiment into graphical depictions of consituent Liouville-space pathways greatly facilitates physical interpretation. Although such pathways may be depicted as in Fig. 5(c) [45, 46], a far more common visualization is that of double-sided Feynman diagrams, where successive orders of density matrix elements are vertically stacked, and where optical interactions are depicted as left-pointing or right-pointing arrows [Fig. 5(d)]. Much has been written about these diagrammatic representations in the MDCS literature, and the reader is referred to Refs. [24, 42, 47–49] for more information.

Finally, it should be noted that the "coherence → population → coherence" mantra should be handled with care in the realm of semiconductor physics because repeated interactions with isolated pulses (e.g., population terms arising solely from a sample's interactions with the first pulse) do exist, and they play an important role in the treatment of certain many-body effects. A satisfactory model of excitation-induced dephasing (EID) and excitation-induced shift (EIS) effects in GaAs quantum wells can only be obtained, for example, after taking these types of terms into account [50]. Inclusion of these effects typically make the response intrinsically non-perturbative and thus require numerical calculations [51]. Moreover, such higher-order EID and EIS effects are among the dominant spectroscopic features in systems like quantum wells and atomically thin transition metal dichalcogenides as discussed later on in Sections 3 and 5. This makes detailed excitation beam power dependences very important in nonlinear spectroscopic studies of semiconductors.

3. Gallium arsenide quantum wells

Having established theoretical underpinnings, we proceed in Sections 3–5 with a review of the ways that MDCS has impacted semiconductor physics. The focus shall be on multidimensional measurements and therefore neglects some of the time-resolved four-wave-mixing literature upon which MDCS is based. The interested reader is directed to Refs. [4] and [52], where time-resolved four-wave mixing literature is more thoroughly discussed.

Gallium arsenide quantum wells were the first semiconductor materials to be studied using MDCS, and they continue to be among the technique's most heavily scrutinized systems. A quantum well is a thin sheet of a semiconductor—typically on the order of 10 nm—sandwiched between slabs of a wider bandgap semiconductor [Fig. 6(a)] to make the potential resemble a finite square well potential in the growth direction. Quantum wells are useful because the well thickness can be readily engineered in the growth process to tune the resonant frequencies of excitons within the well [18]. Beyond this, the confinement has additional advantages for the study and manipulation of excitons in semiconductors because (1) it increases the exciton binding energy, spectrally separating excitons from continuum electrons and holes and increasing the maximum temperature at which excitons remain bound, (2) it splits degenerate excitons into
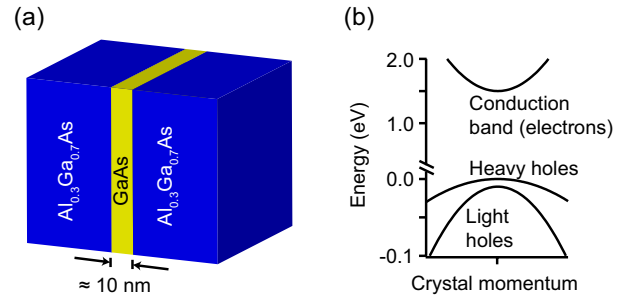
Figure 6 Typical structure of a semiconductor quantum well. (**a**) A narrower bandgap material (in the illustrated case, GaAs) is sandwiched on both sides by a wider bandgap material ($Al_{0.3}Ga_{0.7}As$) to produce one-dimensional quantum confinement. (**b**) Changing the quantum well thickness tunes the resonant frequencies of the excitons within the quantum well. For GaAs, the relevant transitions are between the electronic conduction band and either the heavy-hole or light-hole valence band.

distinct energy bands in a controllable fashion, (3) it increases the exciton dipole moment, thereby increasing the overall strength of light-matter interactions, and (4) the broken translational symmetry along the quantum well growth direction also removes (or in the case of multiple quantum wells, modifies) the exciton-polariton dispersion in this direction [53, 54], leading to interesting tunable polaritonic effects.

Perhaps the largest contribution that MDCS has achieved toward understanding the mechanisms driving exciton formation and dynamics in gallium arsenide quantum wells has been its ability to probe many-body effects. Although such effects can in part be probed using one-dimensional techniques, the techniques leave an incomplete picture of microscopic mechanisms. For example, the classic signature of exciton-exciton correlations in a time-integrated two-pulse four-wave-mixing experiment is the appearance of a signal at negative time delays [55], but it is unclear from such a measurement whether the signal originates from local fields [55], biexcitons [56], excitation-induced dephasing [57, 58], or excitation-induced shift [50]. Both because of its phase-resolved nature and because spectral features are spread out across multiple dimensions instead of just one, MDCS has proven capable of providing a much more stringent constraint on many-body theories [17, 59].

3.1. Many-body signatures in one-quantum spectra

The first studies using MDCS to study many-body physics in semiconductor quantum wells were conducted in the mid-2000s in a series of experiments [60–62] examining a 10-period GaAs quantum well sample consisting of 10-nm-thick GaAs layers separated by 10-nm-thick $Al_{0.3}Ga_{0.7}As$ barriers. The band structure cartoon in Fig. 6(b) illustrates the relevant optical transitions, which are a "heavy-hole" transition at about 1550 meV, and a "light-hole" transition about 10 meV above this.
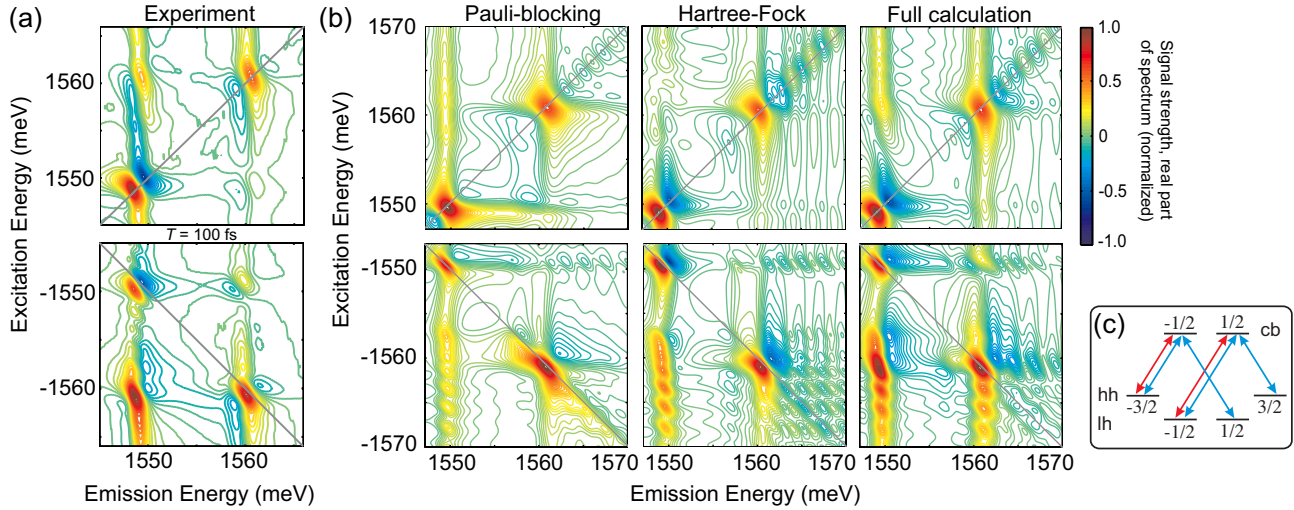
Figure 7 Demonstration of many-body effects in gallium arsenide quantum wells. **(a)** Experimental MDCS measurements of the heavy-hole and light-hole exciton for a 10-period GaAs/Al$_{0.3}$Ga$_{0.7}$As multiple quantum well with 10-nm wells and 10-nm barriers. Data correspond to the real part of a rephasing spectrum (lower panel) and nonrephasing spectrum (upper panel), with co-circular polarization, at an intermediate time delay $T = 100$ fs. **(b)** Simulations of the spectra from (a), with increasingly sophisticated theoretical treatments running from left to right. **(c)** Quantum well level structure, showing the angular momentum states of the conduction band (cb) and the heavy-hole (hh) and light-hole (lh) valence bands. Allowed transitions for co-circular optical polarization are displayed in red. Those for co-linear polarization are displayed in blue. Adapted from Zhang *et al.* [60].

As shown in Fig. 7, MDCS reveals a rich array of spectral features for these two transitions. The two spectra correspond to the real part of the spectral response for rephasing (bottom panel) and nonrephasing (top panel) pulse sequences. Both the rephasing and non-rephasing spectra in Fig. 7(a) exhibit prominent diagonal peaks at about 1549 meV and 1560 meV, which are signatures of absorption at the heavy-hole and light-hole frequencies. The spectra also exhibit cross-peaks, in the rephasing spectrum at (1549,-1560) meV and (1560,-1549) meV, and in the nonrephasing spectrum at (1549,1560) meV and (1560,1549) meV, which are an indication of coherent coupling between the two resonances.

Beyond this, the spectra exhibit a number of other features that indicate a clear influence on the system from many-body effects. For example, the heavy-hole diagonal peak in both the rephasing spectrum and in the nonrephasing spectrum exhibits a phase shift relative to the phase that would be expected for the peak resulting from Pauli blocking in the absence of many-body effects. The MDCS spectrum from a simple three-state system where the nonlinear response is driven by Pauli blocking should be purely real and purely positive at the point of maximum amplitude. In addition, the cross peaks that are clearly evident in both the upper and lower panels of Fig. 7(a) should not normally be expected to have a higher peak amplitude than the peak amplitudes of the diagonal peaks they connect. In fact, as a result of angular momentum selection rules [Fig. 7(c)], such cross peaks should be absent for co-circularly polarized excitation beams without taking the Coulombic interactions between excitons into account because the heavy-hole and light-hole excitons are generated from entirely independent single-particle electronic states.

The importance of many-body effects, as well as insight into their specific nature, is underlined by a comparison between the experimental data from Fig. 7(a), and the left, center, and right columns of Fig. 7(b), which correspond to increasingly sophisticated theoretical treatments of the system based on a microscopic many-body theory using a 1D tight-binding model. As illustrated by the left column of Fig. 7(b) and as discussed in the previous paragraph, Pauli blocking alone cannot adequately replicate the experimental features from Fig. 7(a). The center column, which incorporates Hartree-Fock terms in addition to the effect of Pauli blocking, does a somewhat better job, but a much more satisfactory agreement—even taking into account the inherent limitations of a 1D model—can be obtained by employing a dynamics-controlled truncation scheme incorporating third-order Coulombic correlations [63–65]. Results of this "full" calculation are displayed in the column at right.

The bulk of the data displayed in Refs. [60–62] were acquired using either co-linear or co-circular polarization, which emphasizes the influence of excitation-induced dephasing and excitation-induced shift many-body effects. Probing a GaAs quantum well sample with cross-polarized MDCS pulses (in either cross-linear or cross-circular orientation) opens the possibility of observing and characterizing biexcitons, which are four-particle bound states consisting of two electrons and two holes. Figure 8 shows two measurements on GaAs using co-circular ($\sigma^+\sigma^+\sigma^+\sigma^+$) and cross-linear (XYYX) geometries [66]. Whereas co-circular polarization suppresses the biexciton resonance due to spin dependent selection rules (the biexciton corresponds to an antisymmetric spin configuration), biexcitons are unmistakably visible in the cross-linear polarization spectrum as a shifted peak to the left of the heavy-hole direct peak, which
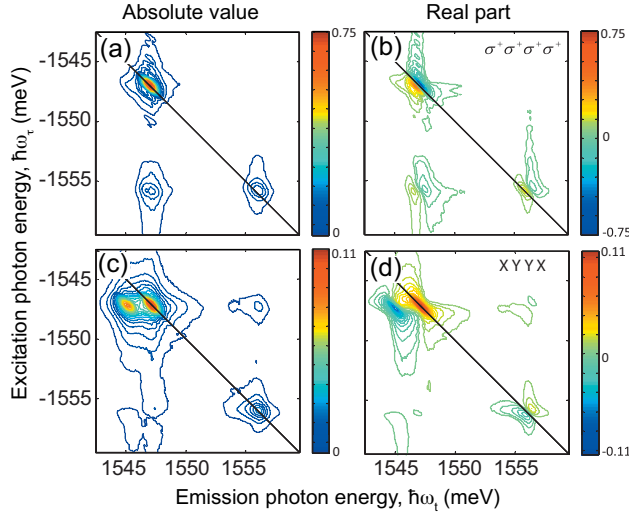
Figure 8 Biexcitons in GaAs. **(a)** Absolute value and **(b)** real part of a rephasing MDCS measurement of a GaAs multiple quantum well with co-circular polarization, in which the biexciton resonance is suppressed. **(c)** Absolute value and **(d)** real part of a rephasing MDCS measurement using cross-linear polarization (XYYX), in which the biexciton is accentuated. Adapted from Bristow *et al.* [66].

is itself suppressed in a cross-polarized geometry. Measurements of the real part of the spectrum show that the sign of the biexciton resonance is negative relative to that of the diagonal resonance, which is an expected consequence of the fact that the biexciton shows up in the spectrum as an excited-state absorption feature.

Although the model behind Fig. 7(b) was constructed using Fermionic creation and annihilation operators, it is worth noting that the strongly dispersive character of the diagonal peaks in Fig. 7(a) can be perhaps more compactly understood through a treatment of excitons as bosons, where the dispersive character of the lineshape arises by a near, but not quite total, cancellation between the interaction pathway for creating an exciton out of the vacuum and the interaction pathway for boosting an exciton from a singly-occupied mode to a doubly occupied mode. Many-body effects break the symmetry of these two processes such that the latter process occurs at a slightly higher frequency than the former process, resulting in an asymmetric phase. Quantitative fits to co-circularly and cross-circularly polarized MDCS measurements in GaAs quantum well have been recently performed, demonstrating that the phase and linewidth of MDCS measurements of quantum wells under both polarization schemes can be understood within a single theoretical framework [67].

3.2. Many-body signatures in multiple-quantum spectra

One-quantum spectra have considerable power to clarify and elucidate many-body interactions in semiconductors, as

already discussed above. For certain types of information, however, even more information can be gleaned by arranging pulses into a two-quantum configuration, as discussed in Section 2.3 and depicted in Fig. 4(c). In the case of GaAs quantum wells, there are no single-exciton states at the two-quantum frequency, so two-quantum measurements give an exclusive and background-free measurement of excitonic interactions.

Although two-quantum MDCS measurements on GaAs quantum wells were preceded by transient four-wave mixing studies [52, 55, 68–72], the extension of the technique into the multidimensional realm has uncovered a number of new and interesting phenomena. In 2009, Stone *et al.* used two-quantum MDCS to directly generate and probe the lifetimes of coherent superposition states between the ground state of GaAs and the biexciton state [73]. The initial results were puzzling because measurements of the biexciton binding energy made by comparing the vertical shift of the two-quantum peak to twice the projection of the peak onto the one-quantum excitation axis gave a different answer from both complementary biexciton binding energy measurements [74–76] and from the binding energy as measured by taking the difference between the biexciton-to-exciton emission peak and the exciton-to-ground-state emission peak.

Shortly thereafter, it was realized that the two-quantum signal was richer in content than had initially been assumed, with a three-dimensional two-quantum measurement dis-
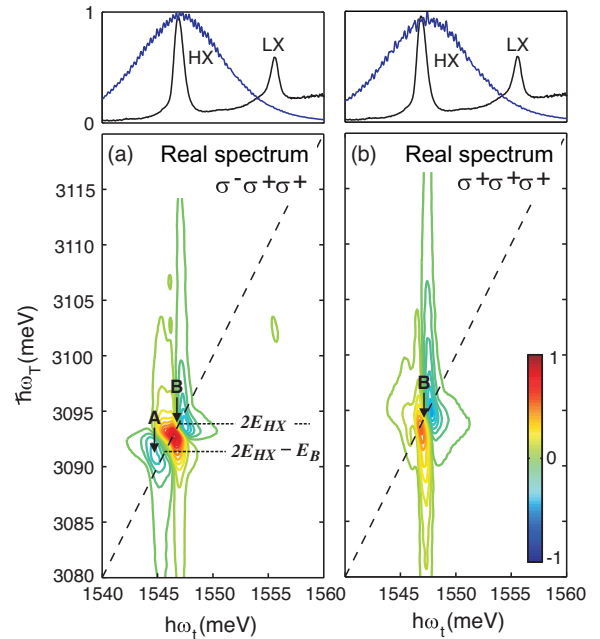
Figure 9 Two-quantum spectra of GaAs quantum wells, with laser bandwidth and center frequency tuned to emphasize the heavy-hole exciton. **(a)** Cross-circular excitation beam polarization, accentuating both the bound biexciton state ("A") and unbound two-exciton state ("B"). **(b)** Co-circular excitation beam polarization, accentuating the unbound two-exciton state only. Adapted from Karaiskaj *et al.* [77].

entangling biexciton coherences that had previously been overlapping [39], and with the real part of two-quantum measurements [77–79] revealing that unbound biexcitons play a significant role in the two-quantum signal in addition to bound biexcitons. An example of a phased two-quantum measurement on a GaAs multiple quantum well [77] is displayed in Fig. 9. Figure 9(a) depicts a measurement using cross-circular polarization ($\sigma^-\sigma^+\sigma^+\sigma^-$), which emphasizes the biexciton resonance. Figure 9(b) depicts a measurement of the same sample using co-circular polarization ($\sigma^+\sigma^+\sigma^+\sigma^+$), in which the signal is exclusively due to unbound excitons.

Two-quantum spectra are just the first of many possible multiple-quantum states that can be probed using MDCS. In follow-up experiments to the results summarized above, Turner and Nelson conducted a series of experiments in which they examined polarizations up to seventh-order in GaAs, revealing tri-exciton coherences in which bound states form among three excitons [80]. Examples of these higher-order electronic correlations are displayed in Fig. 10, where three-quantum coherences are displayed in Figs. 10(a)–10(c), and a four-quantum coherence is displayed in Fig. 10(d) demonstrating a lack of bound-state correlations beyond those at the three-quantum level.

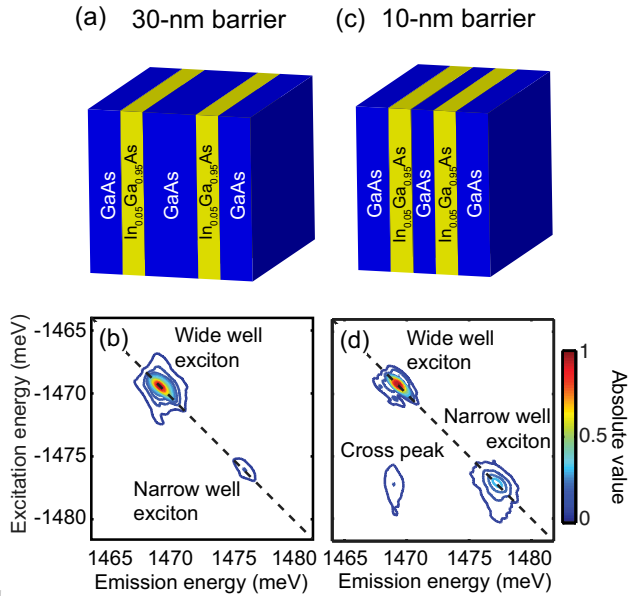## 3.3. Cross peaks as signatures of coupling and hidden resonances

Beyond the ways in which MDCS serves as a means to illustrate the overall importance of many-body effects in quantum wells, the technique has been shown to reveal information about hidden coupling and hidden states. For example, MDCS was used to study coupling effects between wells in InGaAs/GaAs double quantum wells, with $In_{0.05}Ga_{0.95}As$ serving quantum well material, surrounded by layers of wider-band-gap GaAs forming the barrier. InGaAs/GaAs serves as a particularly nice material in these types of studies because strain effects shift the light-hole exciton out of the quantum well, simplifying the spectra corresponding to the remaining heavy-hole excitons in the wells. An understanding of coupling between the wells can be facilitated by making the two wells asymmetric in their thickness, such that excitons corresponding to the wide-well have lower frequencies than excitons primarily situated in the narrow well.

By comparing an asymmetric InGaAs/GaAs double quantum well of this sort with a 30-nm barrier between wells to a more strongly coupled asymmetric InGaAs/GaAs double quantum well with a 10-nm barrier between wells, the authors were able to observe a cross peak that—through further measurements of its characteristics as a function of the intermediate mixing time T and its appearance in two-quantum spectra—was confirmed to originate from excitation-induced dephasing and excitation-induced shift in a similar manner to the way that these two phenomena affect the lineshapes in GaAs/AlGaAs quantum wells. Characteristic spectra corresponding to the 30-nm-barrier sample and the 10-nm-barrier sample are displayed in Fig. 11.
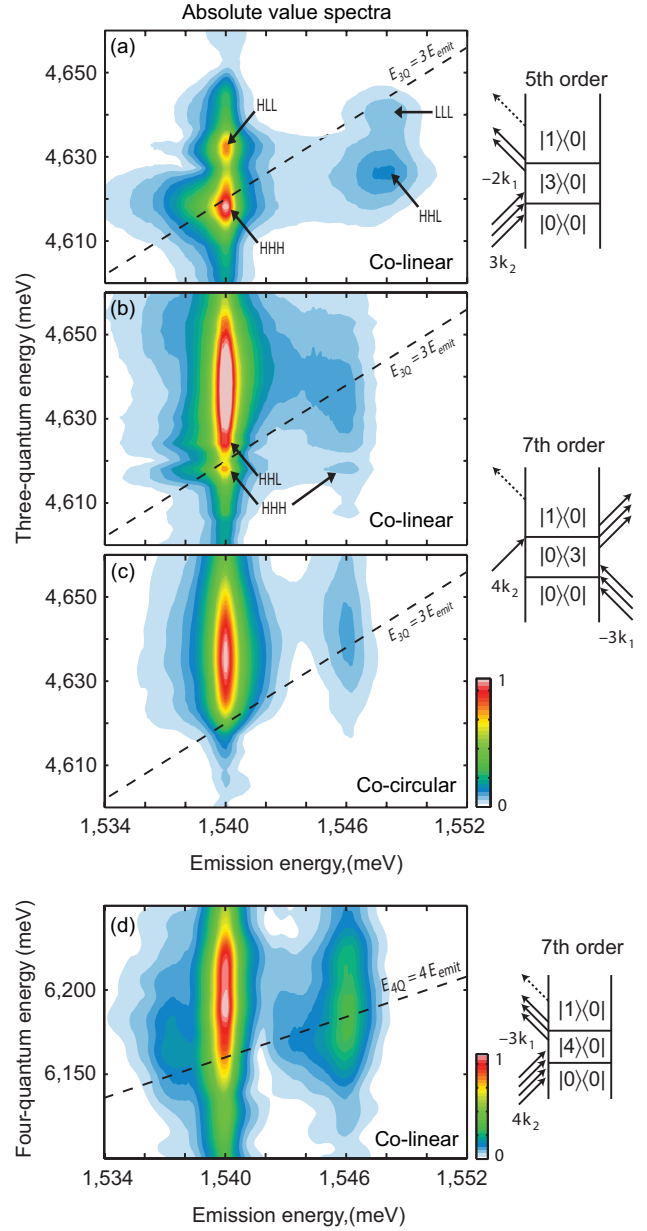
Figure 10 Higher-order multiple-quantum spectra in GaAs. **(a)** Three-quantum coherences, resulting from fifth-order and seventh-order polarizations. **(b)** Four-quantum coherence, from a seventh-order polarization. Adapted from Turner and Nelson [80].

More recently, Tollerud *et al.* performed measurements on uncoupled InGaAs quantum wells, and were able to identify cross-peaks between bright excitons and optically dark indirect barrier excitons within the same well that would not otherwise have been visible [82]. This extra degree of visibility, which is illustrated in Fig. (12), originates from the fact that the brightness of the optically dark excitons is proportional to the fourth power of the dark-state dipole moment, whereas the cross-peak between the dark state and a bright state is proportional to the square of the dark-state

(a) 30-nm barrier **(c) 10-nm barrier**

(b) Wide well exciton

Narrow well exciton

(d) Wide well exciton

Cross peak

Narrow well exciton

Figure 11 Coherent coupling effects in asymmetric InGaAs/GaAs double quantum wells, where one of the wells has a thickness of 10 nm and the other has a thickness of 9 nm. **(a)–(b)** Schematic and absolute value rephasing spectrum for a 30-nm-thick GaAs barrier between wells. **(c)–(d)** Schematic and absolute value rephasing spectrum for a 10-nm-thick GaAs barrier. The cross-peak in the lower left is a signature of coherent coupling. Adapted from Nardin *et al.* [81].

Figure 12 Observation of optically dark indirect barrier excitons through multidimensional coherent spectroscopy. The brightest peaks at upper left corner of the spectrum correspond to optically accessible heavy hole exciton resonances for an uncoupled asymmetric InGaAs/GaAs double quantum well. The cross peaks accentuate interactions with optically dark excitons. Adapted from Tollerud *et al.* [82].
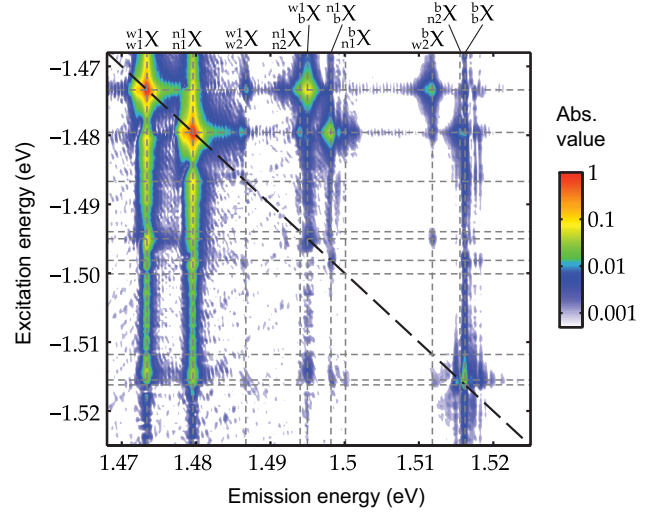
dipole moment multiplied by the square of the much more optically active bright state dipole moment.

The ability of to isolate otherwise murky spectral features though cross-peaks is not restricted to one-quantum spectroscopy techniques. Recently, Tollerud and Davis have demonstrated a optical MDCS analog of two-quantum heteronuclear NMR [10], in which they examined coupling interactions in coupled asymmetric InGaAs/GaAs double quantum wells (8-nm and 10-nm well thickness, 10-nm barrier) using two-quantum spectroscopy, but in which they tuned the bandwidth of their excitation pulses to select out specific excitation pathways. The authors found that the technique allowed them to identify a two-quantum signal associated with GaAs defects that had previously been confused with other interaction induced effects.

3.4. Exciton dynamics at varied mixing times

A fourth area in which MDCS has impacted the field of quantum wells over the course of the past several years has been in its ability to examine not just the static, but also the dynamical evolution of a bath of generated excitons. Dynamics can be observed and characterized by plotting one-quantum spectra (excitation vs. emission frequency) for a variety of different delays of the mixing time T.

In 2012, this experimental scheme was used to characterize the evolution of many-body effects in GaAs/AlGaAs

quantum wells [83]. The authors found that the real part of the lower-energy diagonal peak evolved from an asymmetric to a more symmetric lineshape over the course 10 ps or more, indicating that incoherent, finite-momentum excitons lying outside the light cone play a significant role in relaxation processes.

Two-dimensional rephasing spectra have also been measured as a function of the waiting time T to characterize spectral diffusion effects in GaAs/AlGaAs quantum wells [84, 85]. Spectral diffusion is a process by which memory of resonance characteristics gets lost over time following excitation of a sample by the pump pulse, due (for example) to phonon-assisted exciton spatial migration. The result in MDCS is that inhomogeneously broadened spectral peaks are initially diagonally elongated at small values of T, but become increasingly round at larger values of T.

Spectral diffusion processes are most commonly treated within the Gauss-Markov approximation, which assumes exponential decay dynamics in going from diagonally elongated features to rounder features. By characterizing the spectral features of GaAs quantum wells on T at various temperatures, it was discovered that the Gauss-Markov approximation breaks down for temperatures lower than 70 K [84]. For the lowest temperatures, the shape of the spectral peaks at large T delays become asymmetric to the point where the concept of a cross-diagonal linewidth becomes itself ill-defined outside the context of complicated lineshape features [85]. An example of this, measured on a GaAs quantum multiple quantum well maintained at 5 K, is depicted in Fig. 13. The lineshape of the heavy-hole exciton absolute value spectrum for $T = 0.2$ ps is nearly Gaussian along the diagonal direction, and nearly proportional to the square root of a Lorentzian along the cross-diagonal direc-
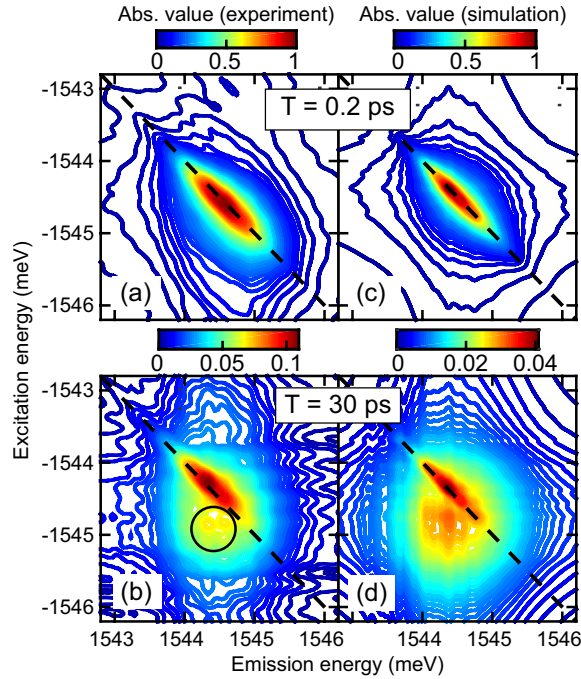
Figure 13 Spectral diffusion for the heavy-hole exciton in a GaAs/Al$_{0.3}$Ga$_{0.7}$As multiple quantum well with 10-nm wells and 10-nm barriers. The sample was measured at 5 K. **(a)–(b)** Experimentally measured spectra. **(c)–(d)** Simulations. Adapted from Singh *et al.* [85].

tion [Fig. 13(a)]. By contrast, the lineshape at $T = 30$ ps [Fig. 13(b)] is noticeably skewed toward the lower left portion of the spectrum (see the solid black circle), and has become almost triangular-shaped in its two-dimensional profile [Fig. 13(b)]. The authors used the measurements to demonstrate that the strong-redistribution approximation for spectral diffusion (in which it is assumed that diffusive processes to higher energies are as likely to occur as those to lower energies) breaks down in addition to the Gauss-Markov approximation at the lowest temperatures. A theoretical simulation could nevertheless still be achieved by solving the two-dimensional Schrödinger equation under random realizations of disordered confinement potentials, and analyzing the average of resulting dynamic localization [Figs. 13(c) and 13(d)].

4. Quantum dots

Semiconductor quantum dots are the zero-dimensional analog of quantum wells, namely, nanocrystals in which the spatial dimensions are reduced to produce exciton quantum confinement effects in not just one spatial dimension, but rather in all three dimensions simultaneously. In turn, this confinement leads to a dramatic flattening of quantum dot dispersion curves and the emergence of well-defined, discretely spaced energy levels. The effects have led to the widespread branding of quantum dots as "artificial atoms," with tunable absorption and emission lines, coupling inter-

actions, and decoherence rates. In industrial applications, quantum dots play a significant role in devices including LED-based displays, semiconductor lasers, and optical filters. Basic research studies of the fundamental properties of quantum dots are ongoing, with many current efforts driven by the desire to use quantum dot nanostructures and devices in quantum computation algorithms and as single-photon sources. In the past several years, MDCS has helped elucidate fundamental properties of quantum dot coherence and dephasing, which are relevant to both applications.

Quantum dots are typically produced through one of three mechanisms: (1) they can occur as a localization phenomenon in disordered quantum wells ("interfacial" or "natural" quantum dots), (2) they can be grown through molecular beam epitaxy on top of an appropriate substrate ("self-assembled" quantum dots), or (3) they they can be grown in solution ("colloidal" quantum dots). We summarize below the impact that MDCS has had in clarifying the physics behind each quantum dot variety, primarily focusing on characterization and manipulation of the first two classes of quantum dots, which have been more widely measured in the low-temperature limit, but also touching briefly on the recent progress in understanding the physics of colloidal dots.

4.1. Identification and characterization of quantum dot excited states

To a sharper degree than for quantum wells, quantum dot studies highlight the power of MDCS to extract homogeneous linewidths from an inhomogeneous ensemble. An example of an MDCS quantum dot spectrum is displayed in Fig. 14, where an ensemble of self-assembled InAs quantum dots was measured at low temperature (10 K) using the rephasing pulse sequence to extract the zero-phonon linewidth [86]. The inhomogeneous broadening exceeded the laser bandwidth in these measurements, but the homogeneous linewidth could be characterized and was measured to be 12 μeV (2.9 GHz) [Fig. 14(a)].

Although the extraction of quantum dot homogeneous linewidths in an inhomogeneously broadened ensemble can also be achieved by other techniques (e.g., transient four-wave mixing [87–89], spectral hole burning [90, 91], and spin noise spectroscopy [92]), MDCS comes into its own for its ability to isolate and characterize exciton, trion, and biexciton properties in a unified experimental framework. For example, information can be gleaned from the aforementioned ensemble of quantum dots by varying the polarization of the excitation pulses, as can be seen in a comparison between Figs. 14(a) and 14(b). Co-linear polarization [HHHH, Fig. 14(a)] emphasizes excitonic resonances, which appear on the diagonal. Similarly to the case of quantum wells, cross-linear polarization [HVVH, Fig. 14(b)] emphasizes the biexcitonic interaction pathway and suppresses the excitonic pathway, making it possible to more clearly identify charged trion resonances on the diagonal, biexcitonic resonances below the diagonal as a third-order response, and even a biexcitonic fifth-order response (due to six-wave
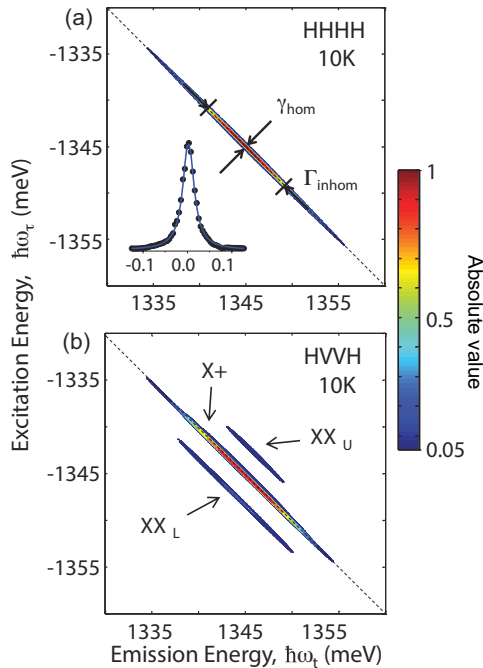
Figure 14 MDCS maps for an ensemble of InAs self-assembled quantum dots. The displayed spectra correspond to the absolute value of a rephasing pulse sequence. The cross-diagonal linewidths γ_{hom} characterizes the homogeneous dephasing rate. The diagonal linewidths Γ_{inhom} are bandwidth-limited. **(a)** Collinear polarization (HHHH), in which excitons are the most prominent phenomena. **(b)** Cross-linear polarization (HVVH), in which biexcitons (XX_L and XX_U) and trions ($X+$) become more prominently featured. Adapted from Moody *et al.* [86].

mixing), above the diagonal. Ensemble measurements of InAs quantum dots have also demonstrated the ability of MDCS to characterize energy-dependent linewidths in an inhomogeneous ensemble, as recently discussed in relation to *p*-shell excitons in Ref. [93].

Another contribution that MDCS has made in understanding the physics of quantum dots is in quantifying biexciton binding energies, and particularly the dependence of the binding energy on quantum dot frequency. An analysis of these effects in both InAs self-assembled quantum dots and in GaAs interfacial quantum dots [94] found that biexciton binding energies exhibit different dependences on emission frequency in the two different types of materials. Whereas the biexciton binding energy increases with emission energy in interfacial quantum dots, it remains an almost perfect constant in self-assembled InAs dots. The latter finding is striking because complementary studies on single InAs quantum dots had found this binding energy to vary [95–97]. The results may indicate that the dependence of biexciton binding energy is obscured by local environment modifications resulting from the necessary etching of mesas or patterning of masks that is required to isolate single dots.

One aspect that eludes ensemble measurements taken even with MDCS is the prospect of measuring quantum

mechanical coupling between dots in different locations. Because interfacial and self-assembled quantum dot ensembles grow randomly, this coupling gets washed out in ensemble measurements even as the homogeneous linewidth is preserved. Coupling has been observed and characterized, however, using frequency-based MDCS in which excitation beams are arranged to impinge upon the sample in collinear geometry [27, 30, 98–103].

Noteworthy work in this area is displayed in Fig. 15 [101]. By combining parallelized collection of four-wave mixing with a collinear series of excitation pulses, it was shown possible to perform hyperspectral imaging, with submicron spatial resolution, of an ensemble of individually identifiable interfacial GaAs quantum dots with results including the observation of individual excitons and biexcitons in individual quantum dots and on coherent coupling between excitons in relatively distant quantum dots. Somewhat surprisingly, the authors found that coupling persisted out to a large inter-exciton distance of almost 1 μm. They attributed the coupling mechanism to a binding interaction mediated by spatially extended states, for example, the oblong green resonance displayed in the lower portion of Fig. 15(d).

Although the dipoles are much weaker, subsequent work has demonstrated that that similar measurements can also be performed on small ensembles of InAs quantum dots. Recently, Mermillod *et al.* used the hyperspectral imaging technique to identify biexcitons and inter-dot coupling effects using an MDCS rephasing pulse sequence [102], and Delmonte *al.* have followed up on this experiment with a study comparing rephasing and two-quantum MDCS pulse sequences [103]. An example of the kinds of observable coupling signatures is displayed in Fig. 16.
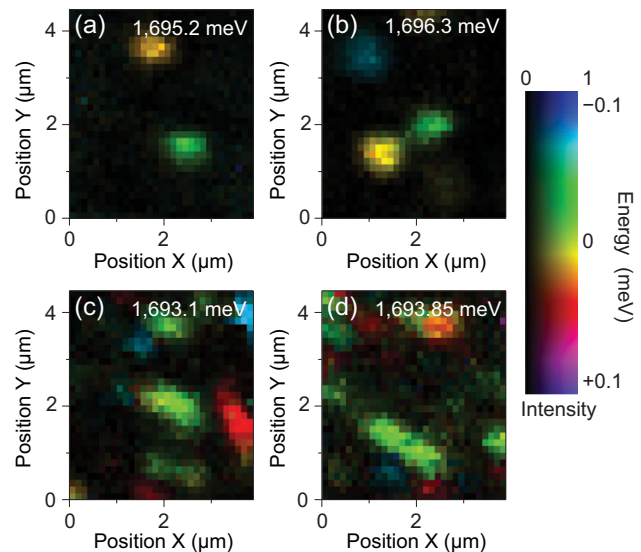
Figure 15 Hyperspectral imaging of the four-wave mixing signal from a GaAs interfacial quantum dot sample. **(a–b)** Images from low-density portions of the sample. **(c–d)** Images from high-density portions of the sample. Adapted from Kasprzak *et al.* [101].
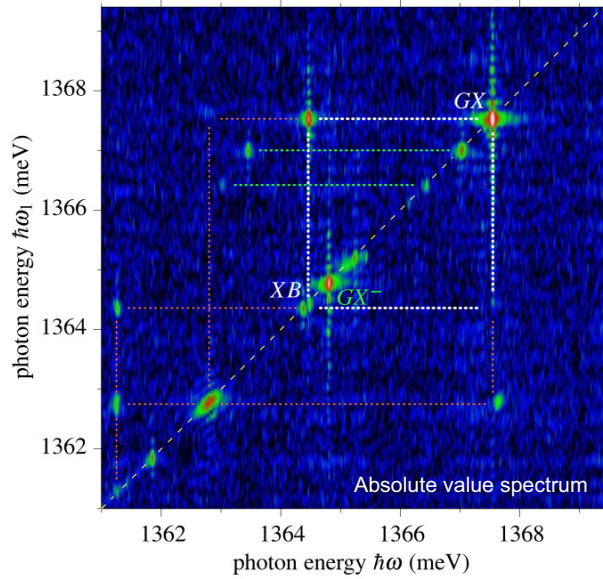
Figure 16 MDCS rephasing spectrum, showing biexcitons and coupling effects pertaining to individual InAs self-assembled quantum dots. The excitation axis is shown on a positive frequency scale, such that the diagonal runs from lower left to upper right. From Mermillod *et al.* [102].

4.2. Progress in coherent control

The identification of MDCS resonances in self-assembled and interfacial quantum dots has opened the door toward being able to manipulate coherent effects between dots and within ensembles of dots in a controlled manner. Among the most prominent recent advances in this direction has been a result in which pulse sequences were used to generate four-wave-mixing and six-wave-mixing effects in a single dot to be able to manipulate the intrinsic coherence of an InAs quantum dot dipole to be able to engineer its coherent emission [104].

The possibility of exerting coherent control of quantum dots can also be scaled up to larger ensembles. For example, by preceding an MDCS experiment with a resonant pre-pulse, Rabi flopping with greater contrast than that visible using transient absorption spectroscopy [106, 107] was observed in an ensemble of InAs quantum dots containing as many as 10 million distinct emitters [105, 108]. Figure 17 shows an example of how this Rabi flopping manifests. In the absense of a pre-pulse, the rephasing spectrum for an ensemble of InAs quantum dots consists of a trion peak along the diagonal, and a biexciton peak to the lower left of the diagonal [Fig. 17(a)]. Applying a pre-pulse of 45 mW drives the ensemble to emit with a biexciton resonance that has moved to the upper right of the diagonal [Fig. 17(b)]. Increasing the pre-pulse power up to 94 mW drives the ensemble back toward its original state [Fig. 17(c)]. The amplitudes of the lower left and upper right peak can be quantified and understood within the context of Rabi oscillations of the exciton-biexciton system, as depicted in Fig. 17(d).
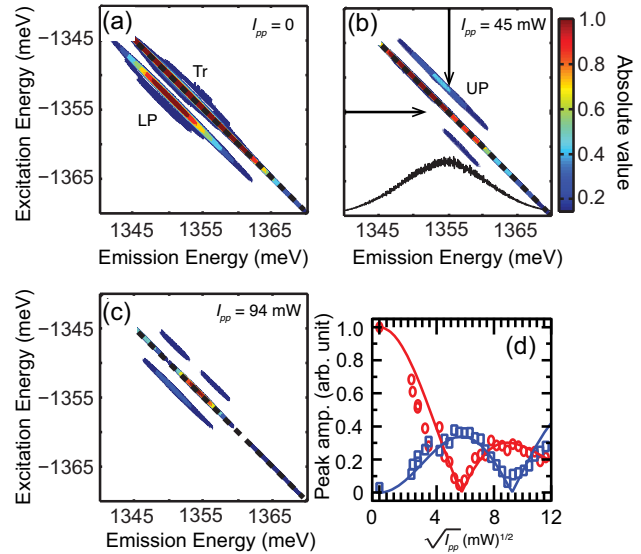

Figure 17 Coherent control of an exciton-biexciton system in an InAs self-assembled quantum dot ensemble. **(a)** Rephasing spectrum in the absense of a pre-pulse. **(b)** Rephasing spectrum with a pre-pulse of 45 mW. **(c)** Rephasing spectrum with a pre-pulse of 94 mW. **(d)** Rabi oscillations of the lower and upper peaks from (a)–(c). The red circles correspond to the amplitude of the lower left peak (LP). The blue squares correspond to the amplitude of the upper right peak (UP). Adapted from Suzuki *et al.* [105].

Beyond inducing Rabi oscillations, Martin and Cundiff have recently shown that it is possible to use a pre-pulse to controllably mediate inter-dot interactions in an ensemble of interfacial quantum dots [30]. By characterizing the sample using two-quantum spectroscopy with excitation pulses of narrow bandwidth, the authors found that inter-dot interactions are normally absent [Fig. 18(c)]. However, interactions could be turned on by applying a pre-pulse resonant with the quantum well wetting layer [Figs. 18(d) and 18(e)].

A potential puzzle in comparing the work of Kasprzak *et al.* [101] to the work of Martin and Cundiff [30] is the question of why interactions were observed in absence of a pre-pulse by the authors of the former paper and yet they were not observed in the absence of a pre-pulse by the authors of the latter paper. Sample variability is one possible explanation. MDCS excitation bandwidth, which was much larger in the work of Kasprzak *et al.*, is an alternate possibility. Further study is required to settle the question more definitively.
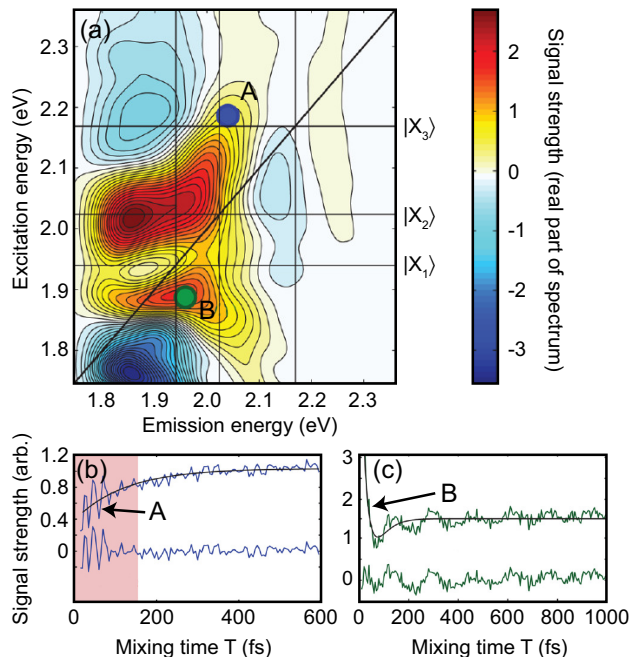
4.3. Colloidal quantum dot MDCS

In comparison to their interfacial and self-assembled epitaxial counterparts, colloidal quantum dots are more tantalizing in their technological potential, but also more experimentally challenging to measure. On one hand, the growth process of colloidal dots in solution is more efficient than the process used to manufacture self-assembled and interfacial dots, and the ability to disperse colloidal dots in solution
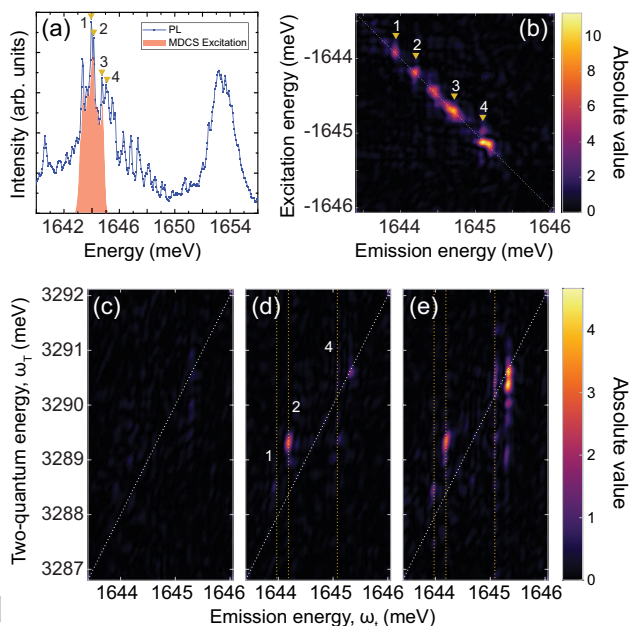
Figure 18 Optical control of interactions in a small ensemble of interfacial quantum dots. **(a)** Photoluminescence measurement of a small ensemble of GaAs interfacial quantum dots, demonstrating the existence of isolated dots and illustrating the bandwidth of the excitation pulses used to generate (b)–(d). **(b)** MDCS rephasing spectrum, depicting four individually identifiable quantum dots. **(c)–(e)** MDCS two-quantum spectra, displayed as a function of increasing pre-pulse power, with the pre-pulse being tuned to the quantum well wetting layer. Adapted from Martin and Cundiff [30].

Figure 19 Room temperature measurements of coherent coupling in CdSe quantum dots. **(a)** One-quantum absorptive spectrum (real part of the sum of rephasing and nonrephasing spectra). The spectrum encompasses three excitonic resonances, respectively labeled $|X_1\rangle$, $|X_2\rangle$, and $|X_3\rangle$. **(b)–(c)** Line-outs as a function of the mixing time T at points A and B from (a) reveal an electronic coherence [shaded pink region of (b)], which can be distinguished from both phonon/solvent relaxation [unshaded portion of (b)] and phonon oscillations [(c)]. Adapted from Caram, *et al.* [110].

opens up a number of possibilities for colloidal quantum dot applications. On the other hand, colloidal quantum dots typically have a larger inhomogeneous broadening than self-assembled or interfacial quantum dots, obscuring features (like electron-phonon coupling effects) with energy scales smaller than that of the inhomogeneous broadening. Beyond this, the increased importance of the material surface in colloidal materials can often lead to "blinking" effects, in which electronic trap states at the dot surface lead to Auger recombination that suppresses individual quantum dot emission for even seconds at a time [109].

Room temperature colloidal quantum dot MDCS studies have been the first set of experiments thus far undertaken, and have already been able to cut through some of the difficulties in understanding physical processes [8]. Among the more prominent systems of study has been CdSe. In 2011, for example, Turner *et al.* used MDCS to report the existence of an electronic zero-quantum coherence between the two lowest lying excitonic states in an ensemble of CdSe quantum dots, lasting about 15 fs [111]. Shortly thereafter, Griffin *et al.* reported that hole relaxation occurs with a timescale very similar to that of the decay reported by Turner [112], offering an alternate explanation for the initial results. Subsequent measurements by Caram *et al.* put the claim of electronic coherences in CdSe on firmer footing by demonstrating the existence of an electronic coherence between the second and third excited states of CdSe, lasting

80 fs (Fig. 19) [110]. More recently, Cassette *et al.* measured room-temperature electronic coherences in a related system of CdSe/CdZnS core/shell nanoplatelets, identifying an unambiguous electronic coherence in the system with a dephasing time of 10–20 fs [113]. The identification was possible because the nanoplatelet system has a cleaner spectrum than the spectrum of CdSe quantum dots (i.e., vibrational coherences and ensemble dephasing do not interfere with the observation of electronic coherences). In all of these systems, the observation of room temperature electronic coherences is important not only because it informs the physics of quantum dot light-matter interactions, but also because of its potential relevance to more complicated systems like photosynthetic light harvesting complexes [114,115].

Very recently, a few MDCS studies have begun to explore the physics of colloidal quantum dots at lower temperatures, which sharpens the relevant spectral features and gives an improved ability to identify intrinsic dephasing rates and electron-phonon coupling. For example, zero-quantum spectroscopy has been used to characterize low-temperature electron-phonon coupling in CdSe quantum dots, with results demonstrating an important role for non-Markovian dynamics CdSe in quantum dot spectral diffusion [116].

5. Transition metal dichalcogenides

Among the most exciting semiconductor discoveries of the past decade has been the discovery of a direct bandgap optical transition in single-layer versions of the transition metal dichalcogenides (TMDs) [117, 118]. Such materials exhibit the chemical form MX_2, where the most common elemental components are M = Mo or W, and X = S or Se. Single-layer TMDs exhibit a number of optical properties not shared by their many-layer parent compounds, including spin-valley coupling effects in the lowest energy excitations, exceptionally large optical interaction dipole moments, and deeply bound excitons with binding energies on the order of several hundred meV. TMD structures and heterostructures hold potential in a number of opto-mechanical applications, includingm atomically thin transistors and sensors [119] and valleytronic nanolasers and LEDs [120]. Because excitonic interactions are of paramount importance in TMDs [19], MDCS is uniquely poised to elucidate interactions in a way that neither linear measurements (like photoluminescence) nor one-dimensional nonlinear measurements (like pump-probe spectroscopy) have been able to achieve.

Among the first MDCS measurements on the TMDs were 2D rephasing spectra, performed first by Moody, et al., aimed at extracting the homogeneous linewidth of WSe_2 [121]. By probing both the temperature and excitation density dependence of a CVD-grown sample of WSe_2 on sapphire, the authors demonstrated that the exciton resonance in WSe_2 exhibits a significant degree of inhomogeneity [Fig. 20(a)], notably hiding the intrinsic homogeneous linewidth in simpler measurements like photoluminescence.

As is the case with the excitons in more established materials like GaAs and ZnSe, the authors observed a strong excitation induced dephasing (EID) in WSe_2 [Fig. 20(b)], which they interpreted as an indication that many-body effects play a significant role in the nonlinear optical signature of the TMDs. Notably, when EID effects are normalized according to inter-exciton separation and exciton Bohr radius, the interaction broadening for WSe_2 turns out to be significantly larger than it is for either GaAs or ZnSe in either bulk or quantum well form. Such strong interactions might be explained by a reduced degree of dielectric screening in two-dimensional materials as opposed to three-dimensional materials.

Quantitative measurements of the homogeneous linewidth [Figs. 20(c) and 20(d)] in the limit of both low excitation density and temperature led to an extrapolated linewidth of 1.6 ± 0.3 meV, leading to a coherence time of $T_2 = 410 \pm 5$ fs. Strikingly, this is almost exactly twice the population relaxation time, which was measured at $T_1 \approx 200$ fs. Such a relationship between T_1 and T_2 is expected for a system with population-decay-limited dephasing, but markedly different from traditional semiconductors. In GaAs quantum wells, for example, typical population times are significantly longer than their corresponding dephasing times [122].

The $T_2 = 2T_1$ relationship between coherence and population decay times has more recently been corroborated by Jakubczyk et al. [123], where the authors probed the dynamics of an exfoliated monolayer sample of $MoSe_2$ on
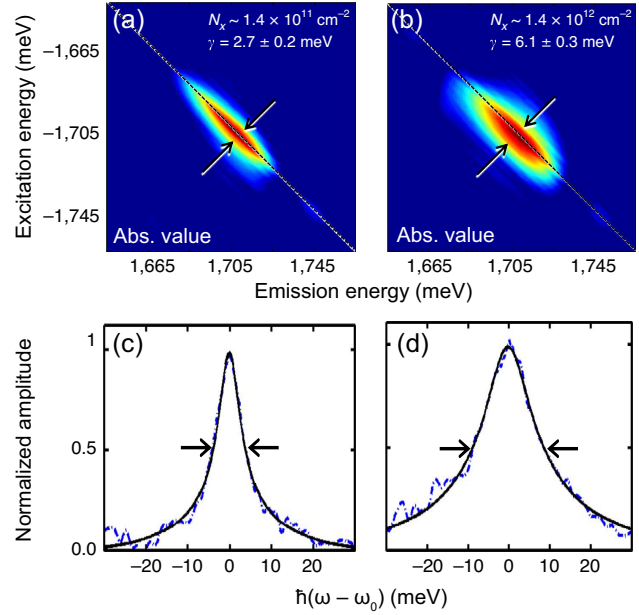
**Figure 20** MDCS spectra of the bright valley exciton in WSe_2 (one-quantum spectrum, rephasing pulse sequence). **(a)** Low excitation density. **(b)** High excitation density. **(c)** Cross-diagonal amplitude profile from (a). **(d)** Cross-diagonal amplitude profile from (b). Adapted from Moody et al. [121].

a Si/SiO_2 substrate using a collinear MDCS experiment with excitation pulses exhibiting a greatly reduced spot size of 700 nm. Importantly, the reduction in spot size allowed the authors to confine their excitation spot to within less than the spatial extent of a single flake of monolayer material, and to be able to distinguish portions of the flake that were predominantly charged and predominantly neutral (Fig. 21), contributing to a significantly reduced degree of spectral inhomogeneity than that reported by Moody et al., which was obtained using a spot size of 30 μm. More recent measurements on single-layer exfoliated WS_2 performed by the same group [124] have yielded similar results and conclusions.

The question of the microscopic origin of dephasing and decoherence in the TMDs is of importance for their practical usefulness as quantum materials. One might optimistically hope, for example, that improvements in sample quality might reduce the scattering contributions to the dephasing rate, thereby increasing T_2 and by extension creating a more advantageous set of material properties for coherent information processing. The current measurements indicating that T_1 and T_2 are already related by a factor of 2 suggest that there may not be much more room for improvement in this area. Beyond this, microscopic calculations [121] indicate that radiative decay with a residual T_2 time of 500 fs becomes the dominant dephasing process for completely delocalized excitons in an ideal single-layer WSe_2 crystal. In addition, spectrally integrated photon-echo measurements on a variety of TMD samples in both bulk and monolayer form [125] found little degradation of TMD dephasing rates in monolayer samples as compared to bulk.
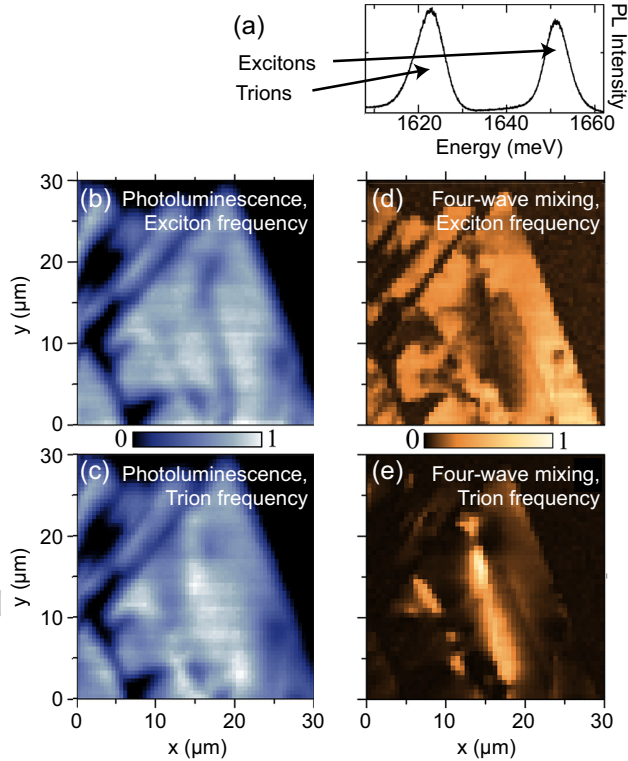
Figure 21 Hyperspectral imaging of an MoSe$_2$ monolayer. **(a)** Photoluminescence measurements reveal two resonances, attributable to neutral bound excitons and charged trions in the sample. **(b)–(c)** Spatially resolved images of this photoluminescence at the resonant frequencies of the exciton [1650 meV, panel (b)] and of the trion [1625 meV, panel (c)] reveal charged and neutral regions of the sample in real space. **(d)–(e)** The contrast is more dramatic, and the spatial resolution sharper, for spatially resolved images of resonant four-wave mixing at the same frequencies. Adapted from Jakubczyk *et al.* [123].

between diagonal exciton and trion resonances [Fig. 22(a)] that oscillates in intensity as the intermediate delay time T is varied. Wider bandwidth studies using a multiresonant variation MDCS have also demonstrated coupling between excitons originating from different sub-bands, and between excitons and the continuum in a sample of few-layer MoS$_2$ (Fig. 23) [131].

MDCS also opens the possibility of probing the zero-quantum coherences between nearly degenerate excited states, offering a powerful test of the degree to which the excitons with opposite pseudospins and in opposite valleys are able to maintain valley coherence. For example, a study of exciton dynamics in WSe$_2$ [132] recently measured the zero-quantum coherence between excitons in opposite valleys (accessed using MDCS beams with cross-circular polarization) to have a linewidth of 6.9 meV. This is almost twice as broad as the exciton population inverse lifetime of 3.4 meV, measured in the same manner but using co-circular polarization. The results place an important bound on the intervalley coherence time of TMDs.

Finally, MDCS studies have faciliated new ways of accessing higher-order states in TMDs like biexcitons. A number of studies have reported evidence for biexciton reso-
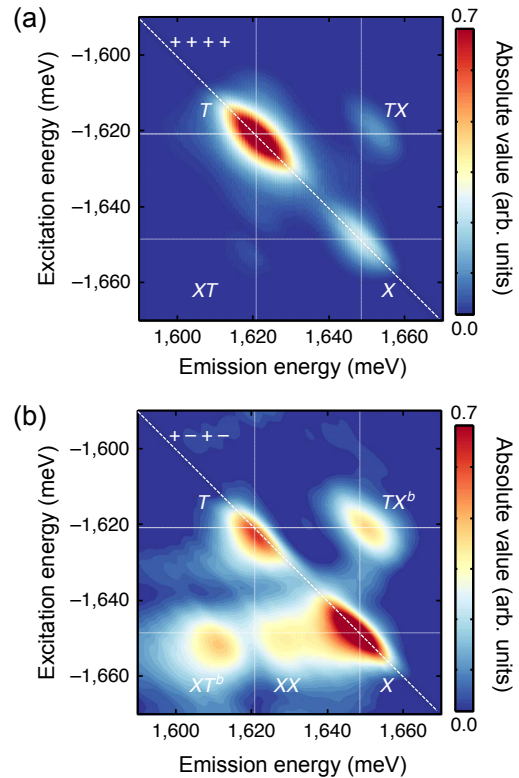
The authors of the photon echo study compared their results to a first-principles model of electron-phonon coupling and concluded that electron-phonon coupling, rather than defect or impurity driven phenomena, are the driving mechanisms in the decoherence rates in TMD monolayers. Ultimately, the issue remains an open question as CVD is known to produce samples that are far from the ideal limit, and the low quantum efficiency of single-layer TMD photoluminescence [126] guarantees that radiative decay processes are still a long way from serving as the dominant decay mechanism. Studies on exfoliated samples that are encapsulated with boron nitride may provide some clarification.

Perhaps the most interesting contributions that MDCS has been able to make in advancing the TMD field have been connected to the technique's ability to reveal signatures of coherent coupling between different resonances. A number of recent studies have investigated the relationship between neutral excitons and charged trions in the materials, most prominently in MoSe$_2$ [123, 127–130], and have found evidence of coherent coupling between the two types of excitations. In MDCS such coupling emerges as a cross-peak

Figure 22 Polarization-resolved MDCS measurements of MoSe$_2$ (one-quantum spectrum, rephasing pulse sequence). **(a)** Co-circular polarization. Exciton (X) and trion (T) resonances are seen to exhibit evidence for coherent coupling in the form of off-diagonal cross-peaks, labeled XT and TX. **(b)** Cross-circular polarization. The cross peak at XX is a manifestation of the biexciton. The cross peaks at TX^b and XT^b are due to charged exciton-trion bound states. Adapted from Hao, *et al.* [130].
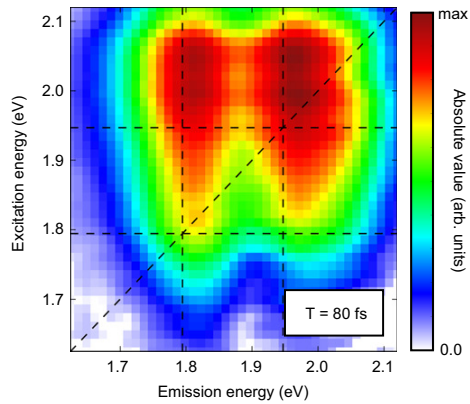
Figure 23 Multiresonant MDCS measurement of exciton transition in few-layer MoS$_2$, depicting coupling effects between the *A* exciton at 1.79 eV and the *B* exciton at 1.94 eV. Adapted from Czech, *et al.* [131].

nances in TMD materials recently [133–137] but there has been some disagreement in the field between theoretical and reported experimental values of biexciton binding energies. A recent study of MDCS that has reveled the presence and binding energy in the biexciton in a much more unambiguous fashion than would be possible using other types of spectroscopy [130]. By illuminating a sample of MoSe$_2$ with cross-circularly polarized light ($\sigma^+\sigma^-\sigma^+\sigma^-$), spectroscopic signatures of the biexciton in MoSe$_2$ emerge that are not visible in a co-circular arrangement of pulses that reveals only exciton resonances, trion resonances, and exciton-trion coupling. As shown in Fig. 22(b), among the most prominent of these is a cross-peak, labeled XX, that has no analog in a spectrum derived from co-circular excitation pulses [Fig. 22(a)]. Comparisons to theory reveal that this peak is a direct signature of the neutral biexciton. Further comparison to theory also demonstrates that the peaks labeled TX^b and XT^b are multi-exciton states corresponding to charged biexciton states [130]. Further analysis indicates that all of these states are intervalley in nature, which—due to the spin-valley coupling inherent in TMDs—may exhibit a number of interesting quantum mechanical properties including entanglement between the pair of valley pseudospins [135].

6. Future directions

In summary, we have reviewed the impact of MDCS in developing a better understanding of the physics of coherent interactions in semiconductors, putting a particular emphasis on the physics of excitons and excitonic interactions. This field, and more generally the field of optical interactions in semiconductors, remains an area of intense active research, and in this final section we summarize potential future directions from the standpoint both of improvements in technology and from the standpoint of potentially interesting material systems of study.

6.1. Technical horizons

A number of efforts are currently underway to improve MDCS resolution, collection efficiency, and versatility. The continuing improvement of pulse laser technologies is opening up new possibilities for conducting MDCS experiments across a wide variety of frequencies. Promising avenues for pursuing these new frequency bands include frequency doubling techniques using second-harmonic generation crystals, increasingly robust and stable optical parametric amplifiers and optical parametric oscillators, and increasingly sophisticated pulse shapers and spatial light modulators [6, 21, 138, 139].

Beyond this, a recent and very exciting development in MDCS technology has been the wedding of the technique with frequency comb technology [140], which holds great promise for improved spectral resolution and collection time. A frequency comb is a spectrum of coherent light with sharply defined "teeth" at discretely spaced frequencies. Such a spectrum corresponds to a pulse train in the time domain with a repetition rate corresponding to the tooth separation in the frequency domain. Combs are appealing in Fourier transform spectroscopy because if a pair of combs with different repetition rates are combined on a single optical path, any sample with which they interact will see the impinging pulses as series of time delayed pulses, where the time delay sweeps through an entire delay cycle at the rate of the difference between the two comb repetition rates [141]. Optical delays for a Fourier transform experiment can in this way be manipulated with exceptionally high cycling rates, giving spectra with exceptional frequency resolution without the need for physically moving parts. Lomsadze and Cundiff have demonstrated nonlinear spectroscopy using such a dual-comb spectroscopy technique [142], and have very recently extended the technique to an MDCS experiment in which one physical delay stages has been combined with a dual-comb detection scheme to observe hyperfine coupling effects in atomic rubidium (Fig. 24) [143]. Extending the dual-comb scenario to a tri-comb arrangement in which three independent frequency combs are all linked has also been recently realized [144] and eliminates physical delay stages altogether.

MDCS technology also holds a number of opportunities for obtaining spectra with increasingly improved spatial resolution. In the past decade, the implementation frequency-tagged four-wave mixing as opposed to momentum-tagged four-wave mixing has brought the resolution of MDCS experiments in the near-infrared regime from a spatial resolution of about 50 μm down to a scale of less than 1 μm. By combining MDCS with near-field techniques, where optical beams are mixed with electronic excitations to generate surface plasmon polaritons with greatly reduced wavelengths, MDCS spatial resolutions could potentially be reduced down to the level of 50 nm or less. In this vein, recent work by Kravtsov *et al.* [145] demonstrating that near-field techniques can be combined with four-wave mixing has proved encouraging.
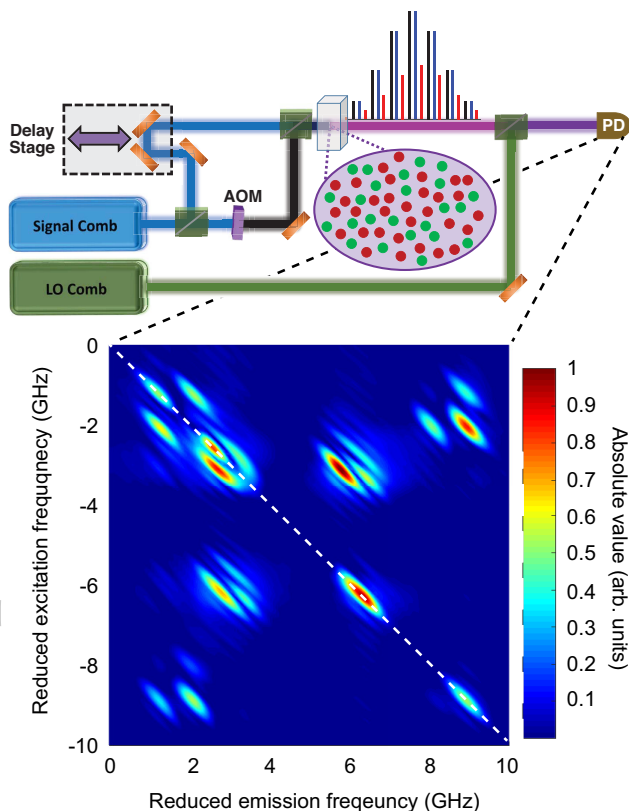
Figure 24 Frequency-comb-based MDCS measurement (rephasing pulse sequence, absolute value spectrum) of coherent coupling effects between the hyperfine states of atomic rubidium. The excitation and emission frequencies are plotted relative to the frequency of a CW reference laser at 377.103258084 THz. Adapted from Lomsadze and Cundiff [143].

6.2. New materials

In tandem with the emerging technological developments in MDCS, the field of semiconductor physics is advancing rapidly, with a great number of new materials having been discovered in the past several years. MDCS is already making inroads toward understanding these materials more effectively.

In quantum well research, a number of studies have developed the ability to embed semiconductor quantum wells within strongly coupled optical cavities, generating new polaritonic excited states, which are hybridized states existing somewhere between being excitons and photons. Exciton-polaritons of these sort form particularly interesting objects of study because of their low mass, and because it has recently been demonstrated that they can be manipulated to form Bose-Einstein condensates under appropriate experimental conditions [146, 147]. MDCS offers a unique window into being able to identify and characterize coupling interactions within these systems.

In quantum dot research, an interesting development has been the demonstration of quantum dot "molecules," which consist of chains of vertically stacked InAs self-assembled quantum dots within an epitaxially grown solid. Much re-

mains to be learned about the way in which dots at different portions of the molecule affect the dots around them, and about the degree to which quantum dot size impacts molecule behavior.

Among the more interesting discoveries in recent TMD research has been the identification of localized TMD states [148–151]. Like their extended-state exciton counterparts, these localized states exhibit spin-valley coupling effects, offering potential for generating new technological links between magnetic and optical effects in semiconducting devices. Among the more promising hopes for these materials is that intervalley coherence times will be longer than have been measured for the excitons in extended excitons states. If sufficiently robust, such states might form important ingredients in quantum computation technology. Beyond this, developments in increasingly sophisticated methods for manufacturing TMD heterostructures have opened up possibilities for generating new types of indirect excitons that straddle neighboring TMD layers of different compositions, and for manipulating exciton screening in interesting ways.

Finally, in recent years there has been growing interest in exploiting the properties of color centers in wide-bandgap semiconductors like diamond, silicon carbide, and boron nitride to create and manipulate coherent electronic states with desirable properties for using in quantum computation and quantum information processing. Because MDCS probes coherent optical properties like dephasing rates and coupling mechanisms, the technique is well-suited to being applied to these types of materials. One such study, characterizing the effects of electron-phonon coupling in nitrogen-vacancy (NV) centers in diamond has already been conducted at room temperature [152]. Low-temperature measurements on the NV centers and related compounds may lead to a great deal of new opportunities and advances.

Christopher L. Smallwood is an assistant professor of physics at San José State University. He received an AB in Physics from Harvard College in 2005. He received a PhD in Physics from UC Berkeley in 2014, where he developed techniques in time- and angle-resolved photoemission spectroscopy to study high-temperature superconductors. He spent two years as a postdoctoral research associate at JILA (University of Colorado and the National Institute of Standards and Technology) from 2014–2016 and two years as a postdoctoral research fellow in the Department of Physics at the University of Michigan from 2016–2018, where he specialized in using ultrafast spec-

troscopy techniques to study light-matter interactions in solid-state media. He is the recipient of a National Research Council postdoctoral Research Associateship award at NIST, and the 2013 Lars Commins Memorial Award in Experimental Physics at UC Berkeley.

Steven T. Cundiff is the Harrison M. Randall Collegiate Professor of Physics at the University of Michigan. He received a BA in Physics from Rutgers University in 1985 and a PhD in Applied Physics from the University of Michigan in 1992. Following his PhD he spent 2 years as a post-doctoral scientist at the University of Marburg, Germany and 2 1/2 years at Bell Labs in Holmdel, New Jersey. In 1997 he moved to JILA, a joint institute between the National Institute of Standards and Technology (NIST) and the University of Colorado, in Boulder, Colorado. From 2004–2009 he was Chief of the NIST Quantum Physics Division. He moved back to the University of Michigan in 2015. He is Fellow of the Optical Society, the American Physical Society, the Institute of Electrical and Electronic Engineers and the American Association for the Advancement of Science. He has received the Meggers Prize from the Optical Society and a Humboldt Research Award.

References

[1] R. Ernst, G. Bodenhausen, and A. Wokaun, Principles of Nuclear Magnetic Resonance in One and Two Dimensions (Clarendon Press, 1990).
[2] P. Hamm and M. Zanni, Concepts and Methods of 2D Infrared Spectroscopy (Cambridge University Press, 2011).
[3] D. M. Jonas, Annu. Rev. Phys. Chem. **54**, 425–463 (2003).
[4] S. T. Cundiff, Opt. Express **16**(7), 4639–4664 (2008).
[5] S. T. Cundiff and S. Mukamel, Physics Today **66**(7), 44 (2013).
[6] B. A. West and A. M. Moran, J. Phys. Chem. Lett. **3**(18), 2575–2581 (2012).
[7] G. Nardin, Semicond. Sci. Technol. **31**(2), 023001 (2016).
[8] E. Cassette, J. C. Dean, and G. D. Scholes, Small **12**(16), 2234–2244 (2016).
[9] G. Moody and S. T. Cundiff, Advances in Physics: X **2**(3), 641–674 (2017).
[10] J. O. Tollerud and J. A. Davis, Laser Photonics Rev. **11**(1), 1600249 (2017).
[11] D. Abramavicius, B. Palmieri, D. V. Voronine, F. Šanda, and S. Mukamel, Chem. Rev. **109**(6), 2350–2408 (2009).
[12] G. D. Scholes, G. R. Fleming, A. Olaya-Castro, and R. van Grondelle, Nature Chemistry **3**(September), 763 (2011).
[13] O. Golonzka, M. Khalil, N. Demirdöven, and A. Tokmakoff, Phys. Rev. Lett. **86**(Mar), 2154–2157 (2001).
[14] J. Zheng, K. Kwak, J. Asbury, X. Chen, I. R. Piletic, and M. D. Fayer, Science **309**(5739), 1338–1343 (2005).
[15] H. Li and S. T. Cundiff, 2d coherent spectroscopy of electronic transitions, in: Advances In Atomic, Molecular, and Optical Physics, edited by E. Arimondo, C. C. Lin, and S. F. Yelin (Academic Press, 2017), chap. 1, pp. 1–48.
[16] P. Y. Yu and M. Cardona, Fundamentals of Semiconductors: Physics and Materials Properties, 3rd edition (Springer, Berlin, 2003).
[17] H. Haug and S. W. Koch, Quantum Theory of the Optical and Electronic Properties of Semiconductors, 2nd edition (World Scientific, River Edge, NJ, 1993).
[18] A. M. Fox, Optical Properties of Solids (Oxford University Press, 2010).
[19] D. Y. Qiu, F. H. da Jornada, and S. G. Louie, Phys. Rev. Lett. **111**, 216805 (2013).
[20] L. Allen and J. Eberly, Optical Resonance and Two-Level Atoms (Dover Publications, 2012).
[21] F. D. Fuller and J. P. Ogilvie, Annu. Rev. Phys. Chem. **66**(1), 667–690 (2015).
[22] M. E. Siemens, G. Moody, H. Li, A. D. Bristow, and S. T. Cundiff, Opt. Express **18**(17), 17699–17708 (2010).
[23] J. D. Bell, R. Conrad, and M. E. Siemens, Opt. Lett. **40**(7), 1157–1160 (2015).
[24] C. L. Smallwood, T. M. Autry, and S. T. Cundiff, J. Opt. Soc. Am. B **34**(2), 419–429 (2017).
[25] P. D. Maker, R. W. Terhune, M. Nisenoff, and C. M. Savage, Phys. Rev. Lett. **8**(Jan), 21–22 (1962).
[26] J. D. Hybl, A. W. Albrecht, S. M. Gallagher Faeder, and D. M. Jonas, Chem. Phys. Lett. **297**(November), 307–313 (1998).
[27] W. Langbein and B. Patton, Opt. Lett. **31**(8), 1151–1153 (2006).
[28] P. F. Tekavec, G. A. Lott, and A. H. Marcus, J. Chem. Phys. **127**(21), 214307 (2007).
[29] G. Nardin, T. M. Autry, K. L. Silverman, and S. T. Cundiff, Opt. Express **21**(23), 28617–28627 (2013).
[30] E. W. Martin and S. T. Cundiff, Phys. Rev. B **97**, 081301 (2018).
[31] P. Tian, D. Keusters, Y. Suzaki, and W. S. Warren, Science **300**(5625), 1553 (2003).
[32] I. D. Abella, N. A. Kurnit, and S. R. Hartmann, Phys. Rev. **141**, 391–406 (1966).
[33] N. H. Ge, M. T. Zanni, and R. M. Hochstrasser, J. Phys. Chem. A **106**, 962–972 (2002).
[34] Y. C. Cheng and G. R. Fleming, J. Phys. Chem. A **112**, 4254–4260 (2008).
[35] J. T. King, J. M. Anna, and K. J. Kubarych, Phys. Chem. Chem. Phys. **13**, 5579–5583 (2011).
[36] M. Khalil, N. Demirdöven, and A. Tokmakoff, Phys. Rev. Lett. **90**(Jan), 047401 (2003).
[37] L. Yang and S. Mukamel, Phys. Rev. Lett. **100**(Feb), 057402 (2008).
[38] S. T. Cundiff, Phys. Chem. Chem. Phys. **16**, 8193–8200 (2014).
[39] D. B. Turner, K. W. Stone, K. Gundogdu, and K. A. Nelson, The Journal of Chemical Physics **131**(14), 144510 (2009).
[40] J. A. Davis, C. R. Hall, L. V. Dao, K. A. Nugent, H. M. Quiney, H. H. Tan, and C. Jagadish, The Journal of Chemical Physics **135**(4), 044510– (2011).
[41] T. Yajima and Y. Taira, J. Phys. Soc. Jpn. **47**(5), 1620–1626 (1979).
[42] R. W. Boyd, Nonlinear Optics, 3 edition (Elsevier, Waltham, MA, 2009).
[43] K. Victor, V. M. Axt, G. Bartels, A. Stahl, K. Bott, and P. Thomas, Z. Phys. B **99**(2), 197–205 (1996).
[44] T. M. Autry, C. L. Smallwood, R. Singh, and S. T. Cundiff p. to be published.

[45] M. Aeschlimann, T. Brixner, A. Fischer, C. Kramer, P. Melchior, W. Pfeiffer, C. Schneider, C. Strüber, P. Tuchscherer, and D. V. Voronine, Science **333**(6050), 1723–1726 (2011).

[46] M. Bauer, A. Marienfeld, and M. Aeschlimann, Prog. Surf. Sci. **90**(3), 319–376 (2015).

[47] T. K. Yee and T. K. Gustafson, Phys. Rev. A **18**, 1597–1617 (1978).

[48] S. Mukamel, Principles of Nonlinear Optical Spectroscopy (Oxford University Press, 1999).

[49] Y. R. Shen, The Principles of Nonlinear Optics (Wiley-Interscience, 2003).

[50] J. M. Shacklette and S. T. Cundiff, Phys. Rev. B **66**(Jul), 045309 (2002).

[51] J. M. Shacklette and S. T. Cundiff, J. Opt. Soc. Am. B **20**(4), 764–769 (2003).

[52] D. S. Chemla and J. Shah, Nature **411**, 549 (2001).

[53] B. Deveaud, F. Clérot, N. Roy, K. Satzke, B. Sermage, and D. S. Katzer, Phys. Rev. Lett. **67**(Oct), 2355–2358 (1991).

[54] J. P. Prineas, C. Ell, E. S. Lee, G. Khitrova, H. M. Gibbs, and S. W. Koch, Phys. Rev. B **61**(May), 13863–13872 (2000).

[55] K. Leo, M. Wegener, J. Shah, D. S. Chemla, E. O. Göbel, T. C. Damen, S. Schmitt-Rink, and W. Schäfer, Phys. Rev. Lett. **65**(Sep), 1340–1343 (1990).

[56] K. Bott, O. Heller, D. Bennhardt, S. T. Cundiff, P. Thomas, E. J. Mayer, G. O. Smith, R. Eccleston, J. Kuhl, and K. Ploog, Phys. Rev. B **48**(Dec), 17418–17426 (1993).

[57] H. Wang, K. Ferrio, D. G. Steel, Y. Z. Hu, R. Binder, and S. W. Koch, Phys. Rev. Lett. **71**(Aug), 1261–1264 (1993).

[58] Y. Z. Hu, R. Binder, S. W. Koch, S. T. Cundiff, H. Wang, and D. G. Steel, Phys. Rev. B **49**(May), 14382–14386 (1994).

[59] M. Kira and S. Koch, Semiconductor Quantum Optics (Cambridge University Press, 2011).

[60] T. Zhang, I. Kuznetsova, T. Meier, X. Li, R. P. Mirin, P. Thomas, and S. T. Cundiff, Proc. Natl. Acad. Sci. U.S.A. **104**(36), 14227–14232 (2007).

[61] T. Zhang, C. N. Borca, X. Li, and S. T. Cundiff, Opt. Express **13**(19), 7432–7441 (2005).

[62] X. Li, T. Zhang, C. N. Borca, and S. T. Cundiff, Phys. Rev. Lett. **96**(5), 057406 (2006).

[63] V. M. Axt and A. Stahl, Z. Phys. B **93**, 195–204 (1994).

[64] V. M. Axt and A. Stahl, Z. Phys. B **93**, 205–211 (1994).

[65] M. Lindberg, Y. Z. Hu, R. Binder, and S. W. Koch, Phys. Rev. B **50**, 18060–18072 (1994).

[66] A. D. Bristow, D. Karaiskaj, X. Dai, R. P. Mirin, and S. T. Cundiff, Phys. Rev. B **79**(Apr), 161305 (2009).

[67] R. Singh, T. Suzuki, T. M. Autry, G. Moody, M. E. Siemens, and S. T. Cundiff, Phys. Rev. B **94**, 081304(R) (2016).

[68] K. B. Ferrio and D. G. Steel, Phys. Rev. B **54**(Aug), R5231–R5234 (1996).

[69] T. F. Albrecht, K. Bott, T. Meier, A. Schulze, M. Koch, S. T. Cundiff, J. Feldmann, W. Stolz, P. Thomas, S. W. Koch, and E. O. Göbel, Phys. Rev. B **54**(Aug), 4436–4439 (1996).

[70] P. Kner, W. Schäfer, R. Lövenich, and D. S. Chemla, Phys. Rev. Lett. **81**(Dec), 5386–5389 (1998).

[71] W. Langbein and J. M. Hvam, Phys. Rev. B **61**(Jan), 1692–1695 (2000).

[72] W. Langbein, T. Meier, S. W. Koch, and J. M. Hvam, J. Opt. Soc. Am. B **18**(9), 1318–1325 (2001).

[73] K. W. Stone, K. Gundogdu, D. B. Turner, X. Li, S. T. Cundiff, and K. A. Nelson, Science **324**(5931), 1169–1173 (2009).

[74] K. H. Pantke, D. Oberhauser, V. G. Lyssenko, J. M. Hvam, and G. Weimann, Phys. Rev. B **47**(Jan), 2413–2416 (1993).

[75] H. Wang, J. Shah, T. Damen, and L. Pfeiffer, Solid State Communications **91**(11), 869–874 (1994).

[76] D. Birkedal, J. Singh, V. G. Lyssenko, J. Erland, and J. M. Hvam, Phys. Rev. Lett. **76**(Jan), 672–675 (1996).

[77] D. Karaiskaj, A. D. Bristow, L. Yang, X. Dai, R. P. Mirin, S. Mukamel, and S. T. Cundiff, Phys. Rev. Lett. **104**(Mar), 117401 (2010).

[78] K. W. Stone, D. B. Turner, K. Gundogdu, S. T. Cundiff, and K. A. Nelson, Acc. Chem. Res. **42**(9), 1452–1461 (2009).

[79] S. T. Cundiff, T. Zhang, A. D. Bristow, D. Karaiskaj, and X. Dai, Acc. Chem. Res. **42**(9), 1423–1432 (2009).

[80] D. B. Turner and K. A. Nelson, Nature **466**(7310), 1089–1092 (2010).

[81] G. Nardin, G. Moody, R. Singh, T. M. Autry, H. Li, F. Morier-Genoud, and S. T. Cundiff, Phys. Rev. Lett. **112**, 046402 (2014).

[82] J. O. Tollerud, S. T. Cundiff, and J. A. Davis, Phys. Rev. Lett. **117**(Aug), 097401 (2016).

[83] D. B. Turner, P. Wen, D. H. Arias, K. A. Nelson, H. Li, G. Moody, M. E. Siemens, and S. T. Cundiff, Phys. Rev. B **85**, 201303 (2012).

[84] R. Singh, G. Moody, M. E. Siemens, H. Li, and S. T. Cundiff, J. Opt. Soc. Am. B **33**(7), C137–C143 (2016).

[85] R. Singh, M. Richter, G. Moody, M. E. Siemens, H. Li, and S. T. Cundiff, Phys. Rev. B **95**, 235307 (2017).

[86] G. Moody, R. Singh, H. Li, I. A. Akimov, M. Bayer, D. Reuter, A. D. Wieck, and S. T. Cundiff, Phys. Rev. B **87**(Jan), 045313 (2013).

[87] P. Borri, W. Langbein, S. Schneider, U. Woggon, R. L. Sellin, D. Ouyang, and D. Bimberg, Phys. Rev. Lett. **87**(Sep), 157401 (2001).

[88] W. Langbein, P. Borri, U. Woggon, V. Stavarache, D. Reuter, and A. D. Wieck, Phys. Rev. B **70**(Jul), 033301 (2004).

[89] P. Borri, W. Langbein, U. Woggon, V. Stavarache, D. Reuter, and A. D. Wieck, Phys. Rev. B **71**(Mar), 115328 (2005).

[90] P. Palinginis, H. Wang, S. V. Goupalov, D. S. Citrin, M. Dobrowolska, and J. K. Furdyna, Phys. Rev. B **70**(Aug), 073302 (2004).

[91] J. J. Berry, M. J. Stevens, R. P. Mirin, and K. L. Silverman, Appl. Phys. Lett. **88**(6), 061114 (2006).

[92] L. Yang, P. Glasenapp, A. Greilich, D. Reuter, A. D. Wieck, D. R. Yakovlev, M. Bayer, and S. A. Crooker, Nat. Commun. **5**, 4949 (2014).

[93] T. Suzuki, R. Singh, G. Moody, M. Aßmann, M. Bayer, A. Ludwig, and A. D. Wieck, ArXiv e-prints(August), 1808.07527 (2018).

[94] G. Moody, R. Singh, H. Li, I. A. Akimov, M. Bayer, D. Reuter, A. D. Wieck, A. S. Bracker, D. Gammon, and S. T. Cundiff, Phys. Rev. B **87**(Jan), 041304 (2013).

[95] A. S. Lenihan, M. V. Gurudev Dutt, D. G. Steel, S. Ghosh, and P. Bhattacharya, Phys. Rev. B **69**, 045306 (2004).

[96] S. Rodt, A. Schliwa, K. Pötschke, F. Guffarth, and D. Bimberg, Phys. Rev. B **71**(Apr), 155325 (2005).

[97] A. Schliwa, M. Winkelnkemper, and D. Bimberg, Phys. Rev. B **79**, 075443 (2009).

[98] W. Langbein and B. Patton, Phys. Rev. Lett. **95**(Jun), 017403 (2005).

[99] B. Patton, U. Woggon, and W. Langbein, Phys. Rev. Lett. **95**(Dec), 266401 (2005).

[100] B. Patton, W. Langbein, U. Woggon, L. Maingault, and H. Mariette, Phys. Rev. B **73**(Jun), 235354 (2006).

[101] J. Kasprzak, B. Patton, V. Savona, and W. Langbein, Nat. Photon. **5**, 57–63 (2011).

[102] Q. Mermillod, D. Wigger, V. Delmonte, D. E. Reiter, C. Schneider, M. Kamp, H. S., W. Langbein, T. Kuhn, G. Nogues, and J. Kasprzak, Optica **3**, 377–384 (2016).

[103] V. Delmonte, J. F. Specht, T. Jakubczyk, S. Höfling, M. Kamp, C. Schneider, W. Langbein, G. Nogues, M. Richter, and J. Kasprzak, Phys. Rev. B **96**, 041124 (2017).

[104] F. Fras, Q. Mermillod, G. Nogues, C. Hoarau, C. Schneider, M. Kamp, H. S., W. Langbein, and J. Kasprzak, Nat. Photon. **10**, 155–158 (2016).

[105] T. Suzuki, R. Singh, M. Bayer, A. Ludwig, A. D. Wieck, and S. T. Cundiff, Phys. Rev. Lett. **117**(Oct), 157402 (2016).

[106] P. Borri, W. Langbein, S. Schneider, U. Woggon, R. L. Sellin, D. Ouyang, and D. Bimberg, Phys. Rev. B **66**(Aug), 081306 (2002).

[107] M. Kujiraoka, J. Ishi-Hayase, K. Akahane, N. Yamamoto, K. Ema, and M. Sasaki, App. Phys. Express **3**(9), 092801 (2010).

[108] T. Suzuki, R. Singh, M. Bayer, A. Ludwig, A. D. Wieck, and S. T. Cundiff, Phys. Rev. B **97**(Apr), 161301 (2018).

[109] A. L. Efros and D. J. Nesbitt, Nat. Nanotechnol. **11**, 661 (2016).

[110] J. R. Caram, H. Zheng, P. D. Dahlberg, B. S. Rolczynski, G. B. Griffin, A. F. Fidler, D. S. Dolzhnikov, D. V. Talapin, and G. S. Engel, J. Phys. Chem. Lett. **5**, 196–204 (2014).

[111] D. B. Turner, Y. Hassan, and G. D. Scholes, Nano Lett. **12**, 880–886 (2012).

[112] G. B. Griffin, S. Ithurria, D. S. Dolzhnikov, A. Linkin, D. V. Talapin, and G. S. Engel, The Journal of Chemical Physics **138**(1), 014705 (2013).

[113] E. Cassette, R. D. Pensack, B. Mahler, and G. D. Scholes, Nat. Commun. **6**(01), 6086 (2015).

[114] G. S. Engel, T. R. Calhoun, E. L. Read, T. K. Ahn, T. Mancal, Y. C. Cheng, R. E. Blankenship, and G. R. Fleming, Nature **446**(7137), 782–786 (2007).

[115] E. Collini, C. Y. Wong, K. E. Wilk, P. M. G. Curmi, P. Brumer, and G. D. Scholes, Nature **463**(7281), 644–647 (2010).

[116] A. Liu, D. B. Almeida, W. K. Bae, L. A. Padilha, and S. T. Cundiff, ArXiv e-prints(June), 1806.06112 (2018).

[117] A. Splendiani, L. Sun, Y. Zhang, T. Li, J. Kim, C. Y. Chim, G. Galli, and F. Wang, Nano Lett. **10**, 1271–1275 (2010).

[118] K. F. Mak, C. Lee, J. Hone, J. Shan, and T. F. Heinz, Phys. Rev. Lett. **105**, 136805 (2010).

[119] W. Choi, N. Choudhary, G. H. Han, J. Park, D. Akinwande, and Y. H. Lee, Mater. Today **20**(3), 116–130 (2017).

[120] J. R. Schaibley, H. Yu, G. Clark, P. Rivera, J. S. Ross, K. L. Seyler, W. Yao, and X. Xu, Nat. Rev. Mater. **1**(August), 16055 (2016).

[121] G. Moody, C. Kavir Dass, K. Hao, C. H. Chen, L. J. Li, A. Singh, K. Tran, G. Clark, X. Xu, G. Berghauser,

E. Malic, A. Knorr, and X. Li, Nat. Commun. **6**, 8315 (2015).

[122] X. Fan, T. Takagahara, J. Cunningham, and H. Wang, Solid State Commun. **108**(11), 857–861 (1998).

[123] T. Jakubczyk, V. Delmonte, M. Koperski, K. Nogajewski, C. Faugeras, W. Langbein, M. Potemski, and J. Kasprzak, Nano Lett. **16**(9), 5333–5339 (2016).

[124] T. Jakubczyk, K. Nogajewski, M. R. Molas, M. Bartos, W. Langbein, M. Potemski, and J. Kasprzak, 2D Mater. **5**(3), 031007 (2018).

[125] P. Dey, J. Paul, Z. Wang, C. E. Stevens, C. Liu, A. H. Romero, J. Shan, D. J. Hilton, and D. Karaiskaj, Phys. Rev. Lett. **116**, 127402 (2016).

[126] M. Amani, P. Taheri, R. Addou, G. H. Ahn, D. Kiriya, D. H. Lien, J. W. Ager, R. M. Wallace, and A. Javey, Nano Lett. **16**(4), 2786–2791 (2016).

[127] A. Singh, G. Moody, S. Wu, Y. Wu, N. J. Ghimire, J. Yan, D. G. Mandrus, X. Xu, and X. Li, Phys. Rev. Lett. **112**, 216804 (2014).

[128] A. Singh, G. Moody, K. Tran, M. E. Scott, V. Overbeck, G. Berghäuser, J. Schaibley, E. J. Seifert, D. Pleskot, N. M. Gabor, J. Yan, D. G. Mandrus, M. Richter, E. Malic, X. Xu, and X. Li, Phys. Rev. B **93**, 041401 (2016).

[129] K. Hao, L. Xu, P. Nagler, A. Singh, K. Tran, C. K. Dass, C. Schüller, T. Korn, X. Li, and G. Moody, Nano Lett. **16**(8), 5109–5113 (2016).

[130] K. Hao, J. F. Specht, P. Nagler, L. Xu, K. Tran, A. Singh, C. K. Dass, C. Schüller, T. Korn, M. Richter, A. Knorr, X. Li, and G. Moody, Nat. Commun. **8**, 15552 (2017).

[131] K. J. Czech, B. J. Thompson, S. Kain, Q. Ding, M. J. Shearer, R. J. Hamers, S. Jin, and J. C. Wright, ACS Nano **9**(12), 12146–12157 (2015).

[132] K. Hao, G. Moody, F. Wu, C. K. Dass, L. Xu, C. H. Chen, L. Sun, M. Y. Li, L. J. Li, A. H. MacDonald, and X. Li, Nat. Phys. **12**, 677–682 (2016).

[133] C. Mai, A. Barrette, Y. Yu, Y. G. Semenov, K. W. Kim, L. Cao, and K. Gundogdu, Nano Lett. **14**(1), 202–206 (2014).

[134] G. Plechinger, P. Nagler, J. Kraus, N. Paradiso, C. Strunk, C. Schüller, and T. Korn, Phys. Status Solidi RRL **9**(8), 457–461 (2015).

[135] E. J. Sie, A. J. Frenzel, Y. H. Lee, J. Kong, and N. Gedik, Phys. Rev. B **92**, 125417 (2015).

[136] Y. You, X. X. Zhang, T. C. Berkelbach, M. S. Hybertsen, D. R. Reichman, and T. F. Heinz, Nat. Phys. **11**(6), 477–481 (2015).

[137] J. Shang, X. Shen, C. Cong, N. Peimyoo, B. Cao, M. Eginligil, and T. Yu, ACS Nano **9**(1), 647–655 (2015).

[138] C. h. Tseng, S. Matsika, and T. C. Weinacht, Opt. Express **17**(21), 18788–18793 (2009).

[139] U. Selig, C. F. Schleussner, M. Foerster, F. Langhojer, P. Nuernberger, and T. Brixner, Opt. Lett. **35**(24), 4178–4180 (2010).

[140] J. Ye and S. Cundiff, Femtosecond Optical Frequency Comb: Principle, Operation and Applications (Springer US, 2006).

[141] I. Coddington, N. Newbury, and W. Swann, Optica **3**(4), 414–426 (2016).

[142] B. Lomsadze and S. T. Cundiff, Opt. Lett. **42**(12), 2346–2349 (2017).

[143] B. Lomsadze and S. T. Cundiff, Science **357**, 1389 (2017).

[144] B. Lomsadze, B. C. Smith, and S. T. Cundiff, Nat. Photon. p. in press (2018).

Author Manuscript

[145] V. Kravtsov, R. Ulbricht, J. Atkin, and M. B. Raschke, Nat. Nanotechnol. **11**(5), 459–459 (2016).

[146] J. Kasprzak, M. Richard, S. Kundermann, A. Baas, P. Jeambrun, J. M. J. Keeling, F. M. Marchetti, M. H. Szymańska, R. André, J. L. Staehli, V. Savona, P. B. Littlewood, B. Deveaud, and L. S. Dang, Nature **443**(September), 409 (2006).

[147] R. Balili, V. Hartwell, D. Snoke, L. Pfeiffer, and K. West, Science **316**(5827), 1007–1010 (2007).

[148] A. Srivastava, M. Sidler, A. V. Allain, D. S. Lembke, A. Kis, and A. Imamoglu, Nat. Nanotechnol. **10**, 491 (2015).

[149] Y. M. He, G. Clark, J. R. Schaibley, Y. He, M. C. Chen, Y. J. Wei, X. Ding, Q. Zhang, W. Yao, X. Xu, C. Y. Lu, and J. W. Pan, Nat. Nanotechnol. **10**, 497 (2015).

[150] M. Koperski, K. Nogajewski, A. Arora, V. Cherkez, P. Mallet, J. Y. Veuillen, J. Marcus, P. Kossacki, and M. Potemski, Nat. Nanotechnol. **10**, 503 (2015).

[151] C. Chakraborty, L. Kinnischtzke, K. M. Goodfellow, R. Beams, and A. N. Vamivakas, Nat. Nanotechnol. **10**(May), 507 (2015).

[152] V. M. Huxter, T. A. A. Oliver, D. Budker, and G. R. Fleming, Nat. Phys. **9**, 744 (2013).